American Mineralogist, Volume 86, pages 790–806, 2001

Characterization and comparison of structural and compositional features of planetary quadrilateral pyroxenes by Raman spectroscopy

ALIAN WANG,* BRAD L. JOLLIFF, LARRY A. HASKIN, KARLA E. KUEBLER, AND KAREN M. VISKUPIC

Department of Earth and Planetary Sciences and McDonnell Center for the Space Sciences, Washington University, St. Louis, Missouri 63130, U.S.A.

ABSTRACT

This study reports the use of Raman spectral features to characterize the structural and compositional characteristics of different types of pyroxene from rocks as might be carried out using a portable field spectrometer or by planetary on-surface exploration. Samples studied include lunar rocks, martian meteorites, and terrestrial rocks. The major structural types of quadrilateral pyroxene can be identified using their Raman spectral pattern and peak positions. Values of Mg/(Mg + Fe + Ca) of pyroxene in the (Mg, Fe, Ca) quadrilateral can be determined within an accuracy of ±0.1. The precision for Ca/(Mg + Fe + Ca) values derived from Raman data is about the same, except that corrections must be made for very low-Ca and very high-Ca samples. Pyroxenes from basalts can be distinguished from those in plutonic equivalents from the distribution of their *Mg′* [Mg/(Mg + Fe)] and Wo values, and this can be readily done using point-counting Raman measurements on unprepared rock samples. The correlation of Raman peak positions and spectral pattern provides criteria to distinguish pyroxenes with high proportions of non-quadrilateral components from (Mg, Fe, Ca) quadrilateral pyroxenes.

INTRODUCTION

Laser Raman spectroscopy is well suited for characterization of materials on the surfaces of planets, satellites, and asteroids (Wang et al. 1995). Raman spectroscopy can be used to identify unambiguously most of the rock forming minerals. It can provide additional information on structural and compositional variations for many mineralogical groups, and many rock types can be inferred from sequences of Raman spectra. This technique can also be used to identify reduced carbon down to ~50 ppm in favorable cases (Wdowiak et al. 1997; Wang et al. 2001) as well as other organic species pertinent to the detection of extraterrestrial life on other planets (e.g., Edwards et al. 1999; Wynn-Williams and Edwards 2000). In addition, it is now feasible to build a small Raman system as part of a scientific instrument payload for a rover or lander to carry out planetary on-surface analyses. A breadboard model of such a Raman system has been built in our laboratory (Wang et al. 1998), and a flight Raman system is under development (Haskin et al. 2001). Raman spectroscopy has typically been used in mineralogy to elucidate structure. Use of Raman spectroscopy as a primary tool for identification and characterization of minerals in a routine manner under field conditions is new. It is thus important to determine the accuracy with which Raman spectroscopy as a stand-alone field tool can do these tasks, especially on sample surfaces as they are encountered and without special preparation for analysis. In this paper, we show that the pyroxene group of minerals is amenable to such identification and characterization.

The pyroxene group is the most important mineral group in planetary mineral suites in terms of the information recorded about petrogenetic processes (e.g., Papike 1996). Its importance as the major rock-forming silicate on the surface of Mars is indicated by the mineralogy of the shergottite basaltic meteorites (e.g., McSween 1994) and by recent data (the ubiquity of basalt and basaltic andesite) from the Thermal Emission Spectrometer on the Mars Global Surveyor (Christensen et al. 2000). Determining the compositional and structural characteristics of pyroxenes in rocks can be crucial to understanding their petrogenesis. In this paper, we evaluate in particular the feasibility of determining both structure and composition of quadrilateral pyroxene [$(Mg,Fe,Ca)_2Si_2O_6$] using only Raman spectra as would be obtained from on-surface planetary measurements. Such characterization would also be useful in terrestrial field and laboratory investigations.

Raman spectral features of pyroxene have been extensively studied in the past. Etchepare (1970) reported a study using polarized Raman measurements on a single crystal of diopside. He also made preliminary assignments of 28 observed peaks into Si-O stretch, M-O bond vibrations, and silicate chain deformations. The first Raman spectra of lunar pyroxene were obtained by Fabel et al. (1972) and Perry et al. (1972) on samples returned by the Apollo missions. They reported two strong Raman peaks, one in the 1000–1010 cm^{-1} range and the other in the 650–670 cm^{-1} range. Perry et al. (1972) also sug-

* E-mail: alianw@levee.wustl.edu

gested that the frequency shifts of pyroxene Raman peaks might be related to their ferrosilite content. A general discussion of Raman features of lunar pyroxenes by White (1975) assigned the ~1000 cm^{-1} peak to the symmetric stretching vibration of Si-O_{nb} bond in $[SiO_4]^{4-}$ tetrahedra (O_{nb} stands for a nonbridging O atom), and the ~670 cm^{-1} peak to the symmetric stretching vibration of Si-O_b-Si bond in $[Si_2O_6]_n$ chains (O_b stands for a bridging O atom). In general, fewer Raman peaks were identified in experiments than the number of Raman active modes predicted by factor group theory. For example, 30 Raman active fundamental vibrations were predicted for *C*2/*c* monoclinic pyroxene (Rutstein and White 1971), but only 28 peaks were identified for diopside, $CaMgSi_2O_6$ (Etchepare 1970), 21 peaks for α-spodumene, $LiAlSi_2O_6$-I (Sharma and Simons 1981), and 18 peaks for Ca-Tschermakite, $CaAl_2SiO_6$ (Sharma et al. 1983). For protoenstatite, $Mg_2Si_2O_6$, (orthorhombic, space group *Pbcn*), factor group analysis indicates 60 Raman active modes, whereas only 44 Raman peaks were observed in polarized Raman measurements made by Ghose et al. (1994). White (1975) suggested that many of these vibrational modes have similar frequencies, and they can only be distinguished from each other by their polarization dependency. Sharma et al. (1983) indicated that accidental degeneracies, weak peak intensities, and a much smaller pseudo-cell in the crystallographic lattice could be the reasons for these inconsistencies.

In addition to these peak assignment studies, Raman studies of pyroxene have documented changes in Raman spectral patterns and shifts in peak positions produced by variations in structure and composition. Dele-Dubois et al. (1980) published Raman spectra of 17 terrestrial pyroxene specimens (two orthorhombic, eleven monoclinic, and five triclinic) using a micro-Raman spectroscopic technique. This work demonstrated a systematic change in spectral pattern among the structural types, as well as differences in peak positions among the pyroxene specimens within each group. Ohashi and Sekita (1982, 1983) and Sekita et al. (1988) investigated the effects of chemical composition and crystallographic parameters on the Raman peak positions of pyroxenes of a wide variety of compositions, including $LiBSi_2O_6$ (B = Al, Fe, Sc), $NaBSi_2O_6$ (B = Al, Ga, Cr, Fe, V, Ti, Sc, In), $CaBSi_2O_6$ (B = Mg, Fe, Mn), $CaScAlSiO_6$, and $CaAl_2SiO_6$. They found a linear correlation between the frequency of the Si-O_b-Si (or Si-O_b-Al) stretching mode and the Si-Si (or Si-Al) distance in the pyroxene chains. We reported the dependence of three major Raman peak positions on the Mg/(Mg + Fe) ratios of several zoned lunar pyroxenes (Wang et al. 1997) and applied this correlation to determine the cation ratios in pyroxenes in rocks of planetary origins (Wang et al. 1999). A recent study by Huang et al. (2000) reported systematic peak shifts of more than ten Raman active modes as a function of Fe content in 18 natural and 25 synthetic Mg-Fe-Ca quadrilateral pyroxene samples, which they suggested could be used to estimate the major-element composition of this type of pyroxene.

The purpose of our study of pyroxene is to develop a method to characterize pyroxene for both structure and composition using only the Raman spectra as might be obtained in the field. The primary motivation is to aid on-surface planetary exploration, and from information about pyroxene composition and variability, to gain an understanding of the petrology and the geologic histories of their host rocks. The spectral criteria for distinguishing different pyroxene structures and the use of pyroxene peak positions to obtain compositional information from spectral data were first established by using paired Raman spectra and electron microprobe analyses (EMPA) on pyroxene grains in a lunar rock sample 15273,7039 (Wang et al. 1997). We now have Raman and EMPA data on pyroxene from fourteen geologic settings, including lunar samples, martian meteorites, and terrestrial rocks. Samples include rapidly cooled, basaltic pyroxene and well-equilibrated plutonic and metamorphic pyroxene. These data are used to evaluate and further develop the Raman method of determining pyroxene structures and compositions.

SAMPLES AND ANALYTICAL METHODS

Samples

Table 1 lists the fifteen samples from which our pyroxene spectra were obtained and tells whether a rock fragment, a polished mount, or both were examined by laser Raman spectroscopy. Brief descriptions of each sample are given in the appendix. Lunar KREEP basalt samples provide the basis for our quantitative correlation. ("KREEP"-bearing rocks are enriched in K, rare earth elements, P, and other incompatible elements.) These samples have relatively simple, mostly quadrilateral pyroxene compositions and are devoid of Fe^{3+}. The samples used in this work include KREEP basalt (15273,7039), a KREEP-rich impact melt rock (14161,7062), a magnesian norite (14161,7080), a whitlockite monzogabbro (14161,7373), and a mafic, brecciated lunar meteorite (QUE94281). Two Martian meteorites, Zagami and EETA79001, were examined in the course of this work. Both are basaltic shergottites (e.g., Meyer 1996) and have basaltic composition and mineralogy. The Martian meteorites represent rocks for which we wish to develop predictive capabilities using Raman spectra. They are also affected by shock and are coarser grained than most of the lunar specimens. Their pyroxene compositions are mainly quadrilateral. We have included a set of terrestrial pyroxene-bearing rocks because these provide additional variations in the form of non-quadrilateral components, e.g., acmite, jadeite, and Ca-tschermakite (e.g., Papike and Cameron 1976) (samples S2-123, 1893, 2670, 901, and M32, Table 1). We have not attempted to investigate all possible variations. Single crystals of seven quadrilateral pyroxene samples (Stdpx01-07) were used for simplified polarization Raman measurements. Raman spectra of six non-quadrilateral pyroxene samples (Stdpx08-13) including pyroxmangite, rhodonite, jadeite, spodumene, wollastonite, and omphacite, were also measured. Table 1 shows the source of compositional data (EMPA) for each sample.

Raman measurements and data handling

Three types of Raman measurements were made. (1) Simple polarization measurements were made to enable tentative spectral peak assignments to specific vibrational modes. (2) Ordinary micro-Raman measurements were made on pyroxene grains at locations where chemical analyses were made by

TABLE 1. List of samples and summary of experimental parameters

Sample no., type	Pyroxene type	Raman measurements	Raman system	Source of compositional data*
		Lunar rocks		
15273,7039, polished section	basaltic	33 individual points (calibration set)	S3000–514.5 nm	EMPA_SS
15273,7039 rock chip, rough surface	basaltic	100 point-counting, 34 Px spectra obtained	S3000–514.5 nm	EMPA_DSSS
14161,7062, thin section	basaltic	100 point-counting, 24 Px spectra obtained	S3000–514.5 nm	EMPA_DSSS
14161,7080, thin section	equilibrated	2 individual points	S3000–514.5 nm	EMPA_DSSS
14161,7373, thin section	equilibrated	3 individual points	S3000–514.5 nm	EMPA_DSSS
QUE94281, thin section	equilibrated	6 individual points	S3000–514.5 nm	EMPA_DSSS
		Martian meteorites		
Zagami, rock chip, flat-cut surface	basaltic	Point-counting 3 linear traverses of 117 points and 2 grids of 212 points, 229 Px spectra obtained	HoloLab-5000–632.8 nm	literature, EMPA_DSSL
EETA79001_476 (A) rock chip, broken surface	basaltic	Point-counting: 5 linear traverses of 561 points, 472 Px spectra obtained	HoloLab-5000–632.8 nm	literature, EMPA_DSSL
EETA79001_357 (B) thin section	basaltic	42 individual points	HoloLab-5000 –632.8 nm	EMPA_SS
		Terrestrial rocks		
Stillwater S2-123, thin section	equilibrated	21 individual points, point-counting on 2 grids of 81 points, 77 Px spectra obtained	S3000–514.5 nm HoloLab-5000–632.8 nm	EMPA_DSSS
Lien no. 1893 garnet pyroxenite flat cut surface	un-equilibrated	Point-counting on 1 linear traverse and 1 grid of 106 points, 55 Px spectra obtained	HoloLab-5000 –632.8 nm	Medaris 1980, EMPA_DSSL
Holsnoy BA-48A#2670 jotunite granulite flat cut surface	equilibrated	Point-counting on 1 linear traverse of 56 points, 11 Px spectra obtained	HoloLab-5000–632.8 nm	Rockow et al 1997, EMPA_DSSL
Brushy Mt. no. 901 Pyroxene andesite, flat-cut surface	un-equilibrated	Point-counting on 1 grid of 45 points, 13 Px spectra obtained	HoloLab-5000–632.8 nm	Thompson et al 1986 EMPA_DSSL
Mingxi M32, garnet-spinel lherzolite, thin section	equilibrated	Point-counting on 1 linear traverse of 44 points, 4 Px spectra obtained	HoloLab-5000–632.8 nm	Qi et al 1995, EMPA
Stdpx01…07, single crystals	equilibrated	7 sets of simplified polarized spectra on each crystal	U1000–514.5 nm	EMPA_DSSS
Stdpx08…13, single crystals	PX of Non-quadrilateral	6 individual points	HoloLab-5000–532.2 nm	EMPA_DSSS

* EMPA_SS (EMPA on same spots); EMPA_DSSS (EMPA on different spots of same sample); EMPA_DSSL (EMPA on different samples of same location).

EMPA to determine the relationship between spectral peak position and chemical composition. (3) Point-counting Raman measurements were made on rock chips to simulate the ability of a field instrument (as might be deployed by a planetary rover), with only approximate focus, to provide definitive identification of pyroxene, classify the pyroxene by type, and determine its chemical composition. The details of the experimental methods and the instruments used are described in the appendix.

For all in-focus Raman measurements, especially the calibration set from sample 15273,7039, the Raman peak positions were obtained by a least-squares curve fitting calculation using the deconvolution program of the Grams/32 software package. This calculation uses a Gaussian-Lorentzian mixed peak shape and a linear baseline, and we used the constraint-free iteration option for all parameters (including the peak position, height, width, Gaussian-Lorentzian mixing percentage for each peak, and slope and intercept for a linear baseline) until convergence was attained. This calculation yields a precision for peak positions of better than ± 0.2 cm^{-1}. For the spectra with lower signal to noise ratio obtained by Raman point-counting measurements on rocks, the peak positions were obtained by visually locating the symmetric center of each peak after a baseline subtraction of the raw spectrum. The precision of determining Raman peak position by this method is estimated to be ± 0.5 cm^{-1}.

EMP analyses and data handling

For the electron microprobe analyses, we used a JEOL 733 Superprobe equipped with a backscattered-electron detector, three wavelength-dispersive spectrometers, and Advanced Microbeam automation. For quantitative mineral analyses, the accelerating voltage was 15 kV, the beam current was 30 nA, and the beam diameter was 10–20 μm. We used a combination of silicate- and oxide-mineral standards. X-ray matrix corrections were based on a modified Armstrong (1988) CITZAF routine incorporated into the electron-microprobe software. Coregistration of Raman spots with EMP analyses was made visually using recognizable microscopic features on the thin sections that could be seen in both the Raman and the EMP analyses.

From each pyroxene analysis, the molar ratios of the cations Si^{4+}, Al^{3+}, Ti^{4+} in tetrahedral sites and molar ratios of the cations Mg^{2+}, Fe^{2+}, Ca^{2+}, Mn^{2+}, Al^{3+}, Ti^{4+}, Cr^{3+}, Na^{+} in octahedral sites were calculated using the measured weight percentages of corresponding oxides based on six O atoms per formula unit $(A,B)_2[Si_2O_6]$, as listed in Table 2.

RESULTS AND DISCUSSION

Typical Raman spectra obtained from pyroxenes of the three major structural types (orthorhombic, monoclinic, and triclinic pyroxenoid) are shown in Figure 1. All three types give a generally similar spectral pattern, and this pattern enables us to distinguish pyroxene unambiguously from other minerals (e.g., olivine, feldspar, phosphates, oxides, etc.) even if Raman peaks of more than one mineral are present in a spectrum taken from a rock. As seen in Figure 1, the detailed spectral features can be used to determine structural type and major cation composition. We show the basis for these relationships in the follow-

TABLE 2. Example pyroxene compositions and spectral parameters

Sample	15273, 7039				EETA79001,357				14161, 7080		14161, 7373		QUE94281		
EMP spot no.	Px 1a	Px 5d	Px 3b	Px 2a	no. 2	no. 6	no. 12	no. 18	7080a	7080b	Px 1	Px 4	Px 1	Px 2	Px 4
SiO_2	53.37	49.82	47.53	46.04	50.33	49.46	54.37	52.32	53.18	51.76	49.55	49.48	46.68	50.94	49.38
TiO_2	0.59	1.60	0.94	0.67	0.24	0.52	0.09	0.45	0.93	1.26	0.24	0.76	1.24	0.34	0.79
Al_2O_3	1.79	1.83	1.17	0.95	0.65	0.40	0.53	1.02	1.05	1.46	0.45	1.21	1.07	1.00	1.13
Cr_2O_3	0.75	0.57	0.26	0.18	0.24	0.10	0.53	0.33	0.46	0.57	0.17	0.34	0.04	0.35	0.31
FeO	13.60	18.69	31.89	39.99	22.80	31.39	16.81	18.47	16.58	7.63	33.35	18.09	30.99	27.74	26.63
MnO	0.18	0.34	0.49	0.61	0.73	0.85	0.55	0.61	0.23	0.15	0.57	0.28	0.35	0.42	0.39
MgO	26.79	15.93	7.67	4.99	16.54	10.02	22.96	13.13	25.75	16.16	12.12	10.25	0.73	12.1	8.59
CaO	2.06	10.76	9.17	5.32	6.31	6.80	3.87	13.92	1.88	20.95	3.90	18.73	18.4	7.61	12.8
Na_2O	<0.01	0.05	0.02	<0.01	<0.01	0.11	0.15	0.08	0.01	0.16	0.02	0.13	0.05	0.03	0.05
Oxide sum	99.1	99.6	99.1	98.7	97.8	99.7	99.9	100.3	100.1	100.1	100.4	99.3	99.6	100.5	100.1
Number of cations on the basis of 6 oxygen atoms															
Si^{4+}	1.937	1.902	1.937	1.944	1.966	1.981	1.995	1.986	1.938	1.918	1.968	1.934	1.942	1.980	1.956
Al^{3+}	0.065	0.079	0.055	0.047	0.026	0.010	0.012	0.038	0.044	0.053	0.020	0.046	0.049	0.037	0.049
Ti^{4+}	0.000	0.015	0.006	0.001	0.000	0.012	0.003	0.000	0.010	0.017	0.000	0.005	0.015	0.000	0.004
Tetr. sum	2.002	1.995	1.998	1.992	1.992	2.003	2.010	2.024	1.993	1.988	1.987	1.985	2.006	2.018	2.009
Al^{3+}	0.012	0.003	0.001	0.000	0.004	0.009	0.011	0.008	0.001	0.011	0.002	0.010	0.004	0.009	0.004
Ti^{4+}	0.016	0.031	0.023	0.021	0.007	0.003	0.000	0.013	0.016	0.018	0.007	0.018	0.024	0.010	0.020
Cr^{3+}	0.021	0.017	0.008	0.006	0.007	0.003	0.015	0.010	0.013	0.017	0.005	0.011	0.001	0.011	0.010
Fe^{+2}	0.413	0.597	1.087	1.412	0.745	1.051	0.516	0.586	0.505	0.236	1.108	0.591	1.078	0.902	0.882
Mn^{+2}	0.006	0.011	0.017	0.022	0.024	0.029	0.017	0.020	0.007	0.005	0.019	0.009	0.012	0.014	0.013
Mg^{+2}	1.449	0.907	0.466	0.314	0.964	0.598	1.256	0.743	1.399	0.893	0.717	0.597	0.045	0.701	0.507
Ca^{+2}	0.080	0.440	0.401	0.240	0.264	0.292	0.152	0.566	0.073	0.832	0.166	0.784	0.821	0.317	0.544
Na^{+}	<0.001	0.003	0.001	<0.001	0.000	0.009	0.011	0.006	0.001	0.011	0.002	0.010	0.004	0.002	0.004
Oct. sum	1.997	2.009	2.005	2.016	2.015	1.994	1.978	1.952	2.015	2.023	2.026	2.030	1.989	1.965	1.982
Quadrilateral components corrected for "others"*															
Wo	4.3	24.0	21.9	13.4	14.0	17.4	10.6	27.7	3.8	40.8	8.5	38.7	41.0	19.0	26.7
En	74.5	45.9	23.4	15.7	48.5	30.0	63.3	40.4	70.7	46.8	36.0	30.8	2.4	35.4	26.8
Fs	21.2	30.2	54.6	70.9	37.5	52.7	26.0	31.9	25.5	12.4	55.5	30.5	56.6	45.6	46.4
Mg/(Mg+Fe)	0.78	0.60	0.30	0.18	0.56	0.36	0.71	0.56	0.73	0.79	0.39	0.50	0.04	0.44	0.37
Mg/(Mg+Fe+Ca)	0.75	0.47	0.24	0.16	0.49	0.31	0.65	0.39	0.71	0.46	0.36	0.30	0.02	0.37	0.26
Ca/(Mg+Fe+Ca)	0.04	0.23	0.21	0.12	0.13	0.15	0.08	0.30	0.04	0.42	0.08	0.40	0.42	0.17	0.28
Raman Spectral parameters and derived cation mole fractions															
Raman ID	p7039a1	p7039x	p703zh	p703zc	J2001	J2003	J2002	J1909	p7080a	p7080b	a14px1	a14px4	QPX1aa	QPX2aa	QPX4aa
peak 1 (cm^{-1})	1004	996.5	991.5	990.4	997	992.2	1003	995	1004	999.2		995.2	990.5	994	991.1
peak 2 (cm^{-1})	680.2	665	661.5	659.8	665.8	662.7	676.2	665.9	677.6	665.6	665.5	664.6	657.2	667.2	663
peak 3 (cm^{-1})	337.4	324.2	314.3	308.8	324	315.8	332.9	324.2	335	325.3	321	320.2	303.9	323.2	317.1
Mg/(Mg+Fe+Ca)	0.78	0.39	0.25	0.18	0.40	0.28	0.67	0.41	0.72	0.41	0.38	0.35	0.09	0.43	0.30
Ca/(Mg+Fe+Ca)	–0.02	0.32	0.20	0.11	0.28	0.18	0.04	0.28	0.03	0.33	0.20	0.22	0.09	0.19	0.21

* Correction for others by the method of Lindsley and Anderson (1983).

ing sections. First, we relate the major spectral peaks to vibrational modes. Next, we show the relationship between peak position and cation composition. Then, we quantify the compositional relationship for both basaltic and equilibrated pyroxenes. Finally, we apply the resulting equation to Raman point-counting results with low S/N measured on pyroxenes within rocks to determine how well the method can be used in the field.

Raman spectral patterns and the structural types of pyroxene

We limit this analysis mainly to quadrilateral pyroxenes, i.e., $[(Mg,Fe,Ca)_2Si_2O_6]$. The major structure types of these pyroxenes correspond to the following space groups: $C2/c$ for the diopside-hedenbergite series, augite, and monoclinic high T pigeonite; $P2_1/c$ for low T pigeonite (Brown 1972); and $Pbca$ for the enstatite-orthoferrosilite series. In addition, triclinic pyroxenoids (e.g., pyroxferroite) have the space group of $P\bar{1}$ (Burnham 1971). Table 3 shows the vibrational modes of these pyroxenes that we obtained by factor group analysis (see also Etchepare 1970, White 1975, Sharma et al. 1981, Sharma et al. 1983, Ghose et al. 1994).

For this analysis, we divide the spectrum of any structural type of pyroxene into five Raman-shift regions : R1, 1100–800 cm^{-1} with a strong asymmetric peak near 1000 cm^{-1} and some wide and weak humps on its two wings; R2, 800–600 cm^{-1} with a strong doublet or an asymmetric single peak near 670 cm^{-1}; R3, 450–300 cm^{-1} with a group of strong overlapping peaks; R4, 600–450 cm^{-1} with a group of overlapping peaks of moderate intensities; and R5, below 300 cm^{-1}, with or without a few peaks of moderate intensity. The number of peaks, peak positions, and relative intensities of the peaks in each region are different for pyroxenes of the different structural types and are used to characterize them.

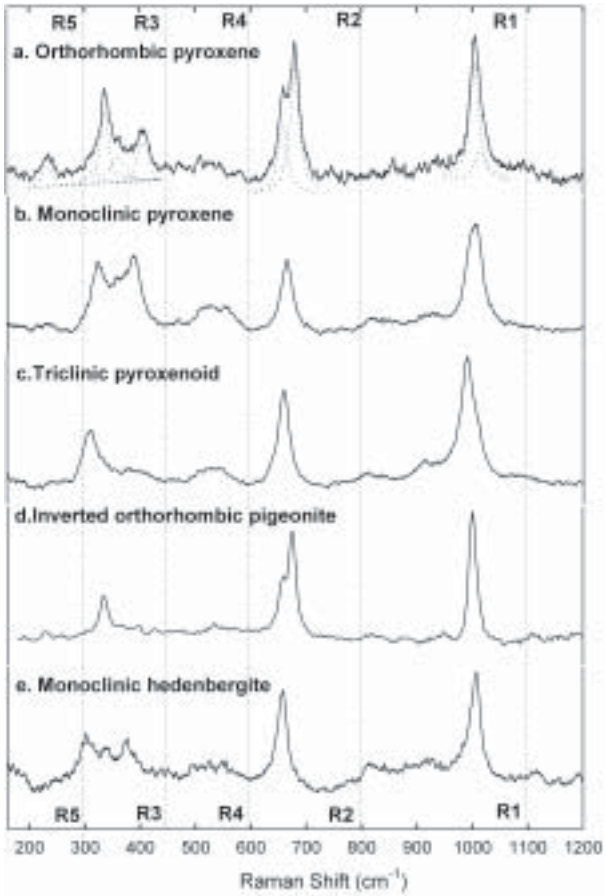

FIGURE 1. Typical Raman spectra of pyroxenes of different structures. Peak shapes in regions R1 and R2 and the number of peaks in region R3 are key to determining pyroxene structural type. Peak positions are key to determining pyroxene cation mole fractions. Note the deconvolved peaks in spectrum a.

Major peak assignments for monoclinic pyroxenes. We begin with the simplest case, *C*2/*c* monoclinic pyroxene, for which the strongest peaks can be most readily assigned. This type of pyroxene has two molecules (20 atoms) per primitive unit cell. Factor group analysis indicates that it has 57 optical vibrational modes. Of these, 30 are Raman active and 27 are infrared active (Rutstein and White 1971). As we see from Table 3, when $[SiO_4]^{4-}$ is considered as an isolated ionic group, it has *Td* symmetry and 9 internal vibration modes. The incorporation of $[SiO_4]^{4-}$ units into a $[Si_2O_6]_n$ chain reduces their symmetry to *Cs* (Bilton et al. 1972), and removes the degeneracy of the E and F_2 modes. Thus, of the 57 optical vibrational modes of *C*2/*c* pyroxene, 36 are internal vibrational modes ($\Gamma_{SiO4\text{-internal vib.}}$) of the four $[SiO_4]^{4-}$ subunits in the two $[Si_2O_6]^{4-}$ chain units in the primitive unit cell. The symmetric stretching mode of Si-O_{nb} in the $[SiO_4]^{4-}$ subunits (at ~1000 cm^{-1}, in spectral region R1) is one of the A_g modes of this group. The relative motions of $[SiO_4]^{4-}$ subunits within the $[Si_2O_6]_n$ chain contribute 9 vibrational modes ($\Gamma_{inner\text{-}chain\ vib.}$), including the A_g symmetric stretching of Si-O_b-Si bonds (at ~670 cm^{-1}, in spectral region R2). The translational motions of the M-site cations contribute 12 vibrational modes ($\Gamma_{cation\text{-}motion}$). These are commonly referred to as crystal lattice modes. Their peaks occur in spectral regions R3 and R5.

Etchepare (1970) detected 13A_g and 15B_g Raman peaks in an oriented single crystal of diopside ($CaMgSi_2O_6$). This suggests that the frequencies of most Raman active modes for *C*2/*c* (C_{2h}^6) pyroxene are separated well enough to be identified. For pyroxenes lacking long-range homogeneity (e.g., polycrystalline pyroxene grains), however, fewer peaks are detected (e.g., 23 according to Sharma and Simons 1981), and for most naturally occurring monoclinic pyroxenes in rocks and soils (Wang et al. 1995, 1997, 1999; Haskin et al. 1997, and this study), only 3–10 peaks are identified under common experimental conditions. This establishes that the intensity differences among the 30 Raman modes are quite large. In all samples, certain modes are strong, so that all samples give dominant peaks in spectral regions R1, R2, and R3. Other modes are weaker and their intensities depend on properties of the particular crystal. Raman spectroscopy is more responsive to changes in long-range order than infrared spectroscopy (White 1975). Therefore, the more localized vibrational modes, which are the least affected by heterogeneities in the crystal (e.g., chain geometric distortion, irregular stacking of subunits, crystal domains, etc.), are the ones that consistently stand out as the major peaks in Raman spectra. These modes are the internal vibrations of the $[SiO_4]^{4-}$ subunits and the localized cation motions. For *C*2/*c* pyroxene, these modes are the Si-O_{nb} bond stretching in the $[SiO_4]^{4-}$ unit (~1000 cm^{-1}, peak 1 in R1), the bridging oxygen stretch in the Si-O_b-Si bond of the $[Si_2O_6]^{4-}$ unit (~670 cm^{-1}, peak 2 in R2), and the simple displacements

TABLE 3. Vibrational modes of four major structural types of pyroxenes

$\Gamma_{SiO4\text{-internal vib.}}$	$\Gamma_{inner\text{-}chain\ vib.}$	$\Gamma_{cation\text{-}motion}$	$\Gamma_{acoustic}$
$[SiO_4]^{4-}$, Td, N = 5, $\Gamma_{optical}$ = 9			
$A^R+E^R+2F_2^{R,IR}$			
Monoclinic pyroxene $M_2Si_2O_6$, *C*2/*c* – C_{2h}^6, N = 20, $\Gamma_{optical}$ = 57			
$9A_g^R + 9\ B_g^R + 9\ A_u^{IR} + 9B_u^{IR}$	$3A_g^R + 3B_g^R + 2A_u^{IR} + B_u^{IR}$	$2A_g^R + 4\ B_g^R + 2A_u^{IR} + 4B_u^{IR}$	A_u+2B_u
Monoclinic pyroxene $M_2Si_2O_6$, *P*21/*c* – C_{2h}^5, N =40, $\Gamma_{optical}$ = 117			
$18A_g^R+18B_g^R+18A_u^{IR}+18B_u^{IR}$	$6A_g^R+6B_g^R+5A_u^{IR}+4B_u^{IR}$	$6A_g^R+6B_g^R+6A_u^{IR}+6B_u^{IR}$	A_u+2B_u
Orthorhombic pyroxene $M_2Si_2O_6$, *Pbca* – D_{2h}^{15}, N = 80, $\Gamma_{optical}$ = 237			
$18A_g^R+18B_{1g}^R+18B_{2g}^R+18B_{3g}^R+18A_u^{IR}$ $+18B_{1u}^{IR}+18B_{2u}^{IR}+18B_{3u}^{IR}$	$6A_g^R+6B_{1g}^R+6B_{2g}^R+B_{3g}^R+6A_u^{IR}+$ $5B_{1u}^{IR}+5B_{2u}^{IR}+5B_{3u}^{IR}$	$6A_g^R+6B_{1g}^R+6B_{2g}^R+B_{3g}^R+6A_u^{IR}$ $+6B_{1u}^{IR}+B_{2u}^{IR}+6B_{3u}^{IR}$	$B_{1u}+B_{2u}+B_{3u}$
Triclinic pyroxenoid $M_7Si_7O_{21}$, $P\bar{1}$ – C_i^1, N = 70, $\Gamma_{optical}$ = 207			
$126A^{R,IR}$	$39A^{R,IR}$	$42A^{R,IR}$	3A

of cations from their equilibrium lattice positions (in R3, within which several peaks may have roughly equal intensity, including peak 3 at ~325 cm^{-1}).

Major peak assignments for orthorhombic pyroxenes and pyroxenoids. There are 60 Raman active modes for $P2_1/c$ pyroxenes, 120 Raman active modes for *Pbca* pyroxenes, and 207 Raman active modes for $P\bar{1}$ pyroxenoids (Table 3). Experimentally observed Raman peaks are nevertheless fewer than ten for those pyroxenes and pyroxenoids as they occur in rocks and soils. Table 3 shows that the cause of the greater number of vibrational modes as compared with the $C2/c$ monoclinic pyroxenes is the enlargement of the primitive unit cells in these pyroxene structures. $P2_1/c$ pyroxenes have double the number of chain units $[Si_2O_6]_n$ per primitive unit cell and therefore double the number of atoms that contribute vibrational modes. For *Pbca* pyroxenes, the numbers are quadrupled. For $P\bar{1}$ pyroxenoids, although the number of chain units per unit cell is kept at two, the size of chain unit increases from $[Si_2O_6]_n$ to $[Si_7O_{21}]_n$, and the number of atoms that contribute vibrational modes increases dramatically. In addition, the low structural symmetry in pyroxenoids causes all vibrational modes to be Raman and infrared active, thus doubling the number of Raman modes. In many cases, however, the frequencies of many vibrational modes in those structures are too similar to resolve under ordinary experimental conditions. Also, the vibrational coupling leading to many of these additional vibrational modes is too weak to produce observable peaks. Thus, a smaller pseudo-cell in the structure of $P2_1/c$, *Pbca*, and $P\bar{1}$ pyroxenes determines their spectral patterns, and the frequencies of the same vibrational modes of neighboring pseudo-cells fall into sets that nearly match the modes of the much smaller structural unit of the monoclinic pyroxenes (White 1975; Sharma et al. 1983, for high-Ca feldspar). Only those vibrational modes that correspond to the strongest modes for monoclinic $C2/c$ pyroxenes (peaks 1, 2, 3: ~1000 cm^{-1}, ~670 cm^{-1}, ~325 cm^{-1}) are thus observed also as the major peaks for the pyroxenes with $P2_1/c$, *Pbca*, and $P\bar{1}$ structures. This results in a similar spectral pattern for all quadrilateral pyroxenes, and the peaks from the same types of vibrations (peaks 1, 2, 3) in pyroxenes with different structures will be used for compositional estimates.

Distinguishing orthorhombic pyroxenes. Despite their general similarities, the different structural units in the different types of pyroxene produce Raman spectral variations useful for structure identification. They are as follows: Both $C2/c$ monoclinic and $P\bar{1}$ triclinic pyroxene have only one type of chain, but *Pbca* orthorhombic and $P2_1/c$ monoclinic pyroxenes have two distinguishable (symmetrically distinct) types of chains (A and B) (Papike et al. 1973). The A chain is more fully extended than the B chain, and the tetrahedra in the A chain are smaller than those in the B chain (Deer et al. 1997; Papike et al. 1973). Chain units $[Si_2O_6]_n^A$ and $[Si_2O_6]_n^B$ thus have different bond angles $\theta_{O3\text{-}Ob\text{-}O3}$ and different bond lengths $L_{Si\text{-}Ob}$ and $L_{Si\text{-}Onb}$. Using enstatite (*Pbca*) as an example, the difference in the angle $\theta_{O3\text{-}Ob\text{-}O3}$ between chains A and B is 22.7° at 20 °C (Deer et al. 1997). The differences in lengths $L_{Si\text{-}Ob}$ of the two bridging bonds Si-O_{3b} are 0.013 Å and 0.029 Å, and the differences in lengths $L_{Si\text{-}Onb}$ of the Si-O_{nb} bond are ~0.007 Å for Si-O1, and ~0.001 Å for Si-O2 (Smyth and Bish 1988). The larger of these differences are sufficient to affect spectral patterns.

Because of these differences in bond length, a doublet near ~670 cm^{-1} (peak 2 in R2, Fig.1a) is observed in the spectra of all orthorhombic pyroxene samples we have studied (enstatite, bronzite, hypersthene, and inverted pigeonite). The lower frequency peak of this doublet sometimes appears as a shoulder on the higher frequency peak, which is always the stronger of the two. The relative intensities of the two peaks of this doublet are independent of crystal orientation in polarization measurements, which suggests that the vibrational modes producing these two peaks belong to the same symmetry class, A_g. This further supports the assignment of this doublet to the Si-O_b-Si stretching vibrations by the chain units of chain A and of chain B, and suggests their vibrations are parallel to each other. In contrast, all of the $C2/c$ monoclinic pyroxene (augite, diopside, hedenbergite) and $P\bar{1}$ triclinic pyroxenoid (pyroxferroite, pyroxmangite) that we have studied show only one Raman peak (~670 cm^{-1}) in spectral region R2, a consequence of the single-chain structure of these pyroxenes. In addition, although *Pbca* and $P2_1/c$ pyroxenes all have doublets in this spectral region, the peak positions of $P2_1/c$ pyroxenes are ~10 cm^{-1} lower than those of *Pbca* pyroxenes owing to compositional differences. Also, the doublet is less well resolved in the spectra of $P2_1/c$ pyroxenes. The orthorhombic structure of inverted pigeonite (*Pbca*) produces a doublet in spectral region R2 (Fig. 1d), very similar to that of high Mg, low Ca *Pbca* pyroxene (Fig. 1a).

If a spectrometer of high enough resolution (3–4 cm^{-1}) is used, most *Pbca* type orthorhombic pyroxenes show a doublet (~1010 and ~1030 cm^{-1}) in spectral region R1 (Fig. 2a). The relative intensities of the two peaks in this doublet vary with

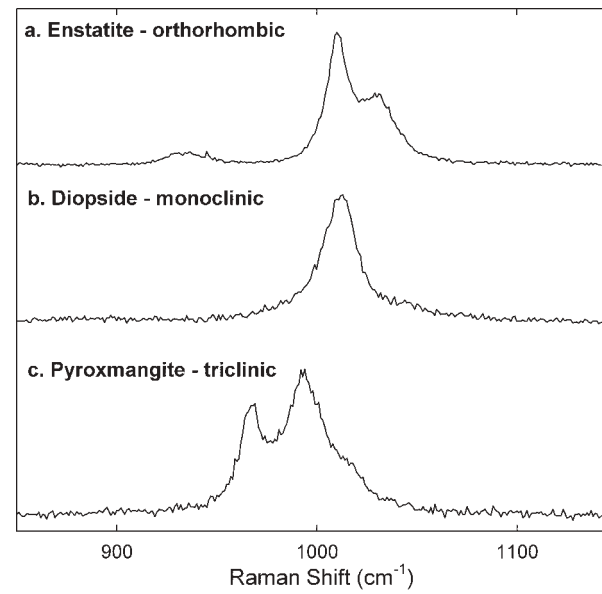

FIGURE 2. High resolution spectra of three structural types of pyroxene in spectral region R1. Note the differences in peak positions and the relative heights of the doublets in spectrum a and spectrum c.

crystal orientation, indicating that they are from vibrational modes with different symmetries. Similarly, the asymmetric shape of peak 1 in R1 of monoclinic pyroxenes (Figs. 1b and 2b) can be deconvolved into two overlapping peaks (~1000 and 1010 cm^{-1}). The relative intensities of these component peaks also depend on crystal orientation, so they, too, must be produced by modes with different symmetries. According to the peak assignments of protoenstatite in R1 (A_g and B_{1g}, B_{2g}, B_{3g}) based on detailed polarization Raman measurements done by Ghose et al. (1994), we cannot attribute the double Raman peaks of *Pbca* pyroxene in R1 to the Si-O_{nb} stretching of the different subunits in chain A and B. Instead, we must assume that the energy difference associated with the difference in bond length of the Si-O_{nb} bonds in the $[SiO_4]^{4-}$ subunits of chains A and B is too small to produce an experimentally resolvable doublet (e.g., in enstatite). In spectra of moderate resolution (5–7 cm^{-1}, such as those in Fig. 1), although the peaks of orthorhombic and monoclinic pyroxenes both have asymmetric shapes in R1, the positions of the higher frequency components are very different, and they form two clearly separated clusters in a plot of peak position against *Mg'* [= Mg/(Mg + Fe)] (Fig. 3 of Wang et al. 1997). Peaks lie above 1020 cm^{-1} for orthopyroxene and near 1010 cm^{-1} for clinopyroxene. This feature is also useful in distinguishing between the pyroxenes of these two structures.

Distinguishing triclinic pyroxenoids. The major Raman spectral difference between triclinic pyroxenoids and other pyroxenes is that the pyroxenoids have the lowest Raman shifts for all peaks (Fig. 1c). The Raman shifts of pyroxferroite peaks are some 10–20 cm^{-1} lower than those of augite, so the distinction between the two is easily made. In addition, about half of the spectra taken from pyroxferroite in lunar sample 15273,7039 have a peak at ~962 cm^{-1}. Figure 2c shows the spectrum of a triclinic pyroxenoid having an additional peak as a low-frequency wing (~974 cm^{-1}) of the Si-O_{nb} stretching A_g peak (see also the triclinic pyroxenoids in the later section on non-quadrilateral pyroxenes). The relative intensity of this peak compared to the main A_g peak (~1000 cm^{-1}) is independent of crystal orientation, suggesting the same A_g symmetry. In the chain units of triclinic pyroxene ($[Si_7O_{21}]_n$ for pyroxmangite, $[Si_5O_{15}]_n$ for rhodonite), the variation in bond length among $[SiO_4]^{4-}$ subunits is larger for Si-O_{nb} bonds (0.045 Å for both pyroxmangite and rhodonite) than for Si-O_b bonds (0.035 Å for pyroxmangite and 0.029 Å for rhodonite, Ohashi and Finger 1975). The vibrational frequencies of Si-O_{nb} stretching of each $[SiO_4]^{4-}$ subunit will be affected by the lengths of its two Si-O_{nb} bonds, in other words, by the degree of asymmetry of the O_{nb}-Si-O_{nb} group (defined as $[(L_{si\text{-}Onb\text{-}mean}-L_{si\text{-}Onb\text{-}A})^2 + (L_{si\text{-}Onb\text{-}mean}-L_{si\text{-}Onb\text{-}B})^2]^{1/2}$). Of the seven $[SiO_4]^{4-}$ subunits in the pyroxmangite chain, there is one $[SiO_4]^{4-}$ subunit which has a relatively larger degree of asymmetric O_{nb}-Si-O_{nb} liaison (0.030–0.032 Å) than other subunits (0.001–0.021 Å). This produces a frequency difference in Si-O_{nb} stretching vibrations that can be resolved by a spectrometer of moderate resolution (more details below). Pyroxferroite found in lunar samples has a chain structure $[Si_7O_{21}]_n$ similar to that of pyroxmangite (Burnham 1971) and a similar highly asymmetric O_{nb}-Si-O_{nb} group in one of its seven $[SiO_4]^{4-}$ subunits. Therefore, an additional peak on the low Raman shift side of the major peak is expected. This appears to have been observed from pyroxferroite in lunar sample 15273,7039. However, because the Raman spectra were taken from a thick section of this lunar rock chip, some spectral contribution from minor phosphate phases cannot be excluded, e.g. apatite. Thus in this study, we assume the typical one-peak pattern in spectral region R1 for pyroxferroite.

Empirical rules in spectral regions R3 and R5, and a flow chart. The spectral patterns in regions R3 and R5 (Fig. 1) are quite different among different pyroxenes. No Raman peak assignments in these regions could be made within the scope of this study. We have nevertheless developed some empirical rules for distinguishing among the three structural types based on the spectra of known samples. Figure 3 is a flow chart of the procedure we have developed for using Raman spectral patterns and peak positions to distinguish among the structure types of quadrilateral pyroxenes.

Raman peak positions and pyroxene compositions

Raman peak positions are related to chemical composition for all three general structural types of pyroxene. We have calibrated these shifts based on Raman peak positions and proportions of major cations as determined by EMP analyses, acquired at the same points. The calibration is based on 33 Raman spectra and EMP analyses obtained from several chemically zoned pyroxene grains in a polished section of lunar rock chip 15273,7039. These spectra include all three structural types, a consequence of the range in the pyroxene chemical compositions. We observed a monotonic shift downward in the peak positions for most Raman peaks with a decrease in *Mg'* [= Mg/(Mg + Fe)].

Precise positions of eight Raman peaks in spectral regions R1, R2, R3, and R5 were obtained for each Raman spectrum by spectral curve fitting. As an example, spectrum "a" in Figure 1 shows the component peaks used for the curve fitting.

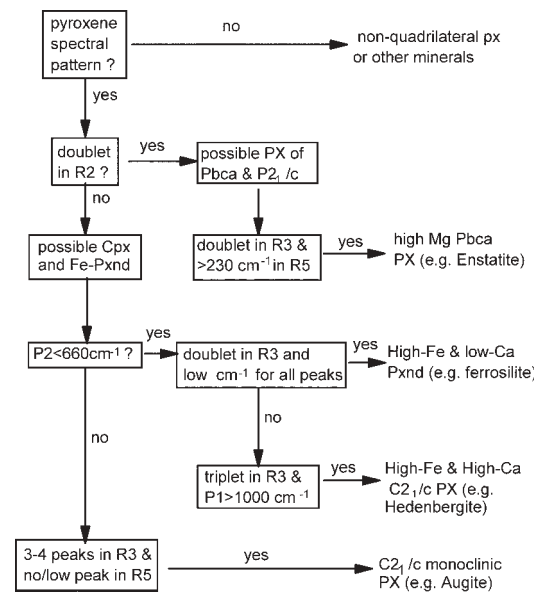

FIGURE 3. This flow chart indicates how to distinguish pyroxene structural type using Raman spectral pattern and peak positions.

The molar ratios of eight cations (Mg^{2+}, Fe^{2+}, Ca^{2+}, Al^{3+}, Ti^{4+}, Cr^{3+}, Mn^{2+}, Na^{+}) at octahedral sites were calculated based on the oxide weight percents obtained by EMP analyses on the same sampling spots. Of these, we have determined that only the major cations, Mg^{2+}, Fe^{2+}, and Ca^{2+}, significantly affect spectral peak positions. We found no obvious correlation for the three cations Al^{3+}, Ti^{4+}, Na^{+} with any Raman peaks for this set of data. We found the effect of Cr^{3+} to be closely correlated with that of Mg^{2+} and the effect of Mn^{2+} to be closely correlated with that of Fe^{2+}. Thus, it is not necessary to treat these two cations independently. Of the eight Raman peaks, only peak 1 (~1000 cm^{-1} in R1), peak 2 (~670 cm^{-1} in R2), and peak 3 (~325 cm^{-1} in R3) correlate well enough with the proportions of Mg^{2+}, Fe^{2+}, and Ca^{2+} to be useful for the determination of cation ratios. In addition, these three peaks are the easiest to observe in spectra when taken out of focus and with low signal to noise, as is common in our point-counting experiments on unprepared sample surfaces (rocks and soils). Figure 4 shows that the three major Raman peaks have a tight linear correlation with molar ratio Mg^{2+}. Their correlation with Fe^{2+} is weaker than that with Mg^{2+}, and shifts in peak position associated with Ca^{2+} are more complex. Raman shifts increase with increasing cation fraction of Mg^{2+} and decrease for both Fe^{2+} and Ca^{2+}. In addition, all three Raman peaks correlate well with each other.

A statistical analysis indicates that the principal dependence of peak positions on cation ratio arises from variation in the mole fraction of Mg^{2+}, and the most direct and strongest effect of cation composition is on the position of peak 3 (~325 cm^{-1}) in R3. As suggested by lattice dynamic modeling (Ghose et al. 1994), the Raman peaks in R3 (including peak 3) are produced by crystal lattice modes involving the displacement of cations and by the mixing of internal and external modes. The strongest correlation between the position of peak 3 with the molar ratios of the cations further suggests that it is produced by the translational motion of the cation in the octahedral sites. In our simple polarization measurements, the relative intensities of peak 2 and peak 3 were independent of crystal orientation, which suggests that the vibrational modes producing these two peaks have at least partially common directions of motion. As the direction of the Si-O_b-Si symmetric stretching vibration (peak 2) is essentially parallel to the axis of the $[Si_2O_6]_n$ chain (the *c* axis of the pyroxene structure), peak 3 is evidently produced by a displacement of M cations in a direction parallel to the axis of $[Si_2O_6]_n$ chain.

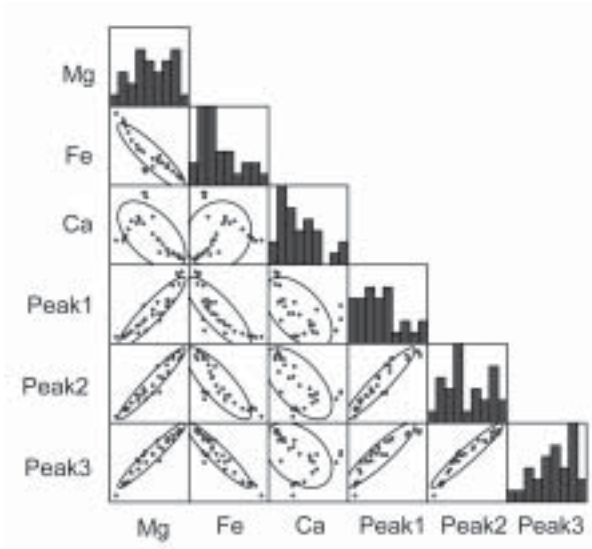

FIGURE 4. Correlations are shown among the positions of three Raman peaks and the molar ratios of the three principal cations in pyroxene octahedral sites. Histograms indicate the number of cases as a function of parameter value.

Consider this cation displacement along the c axis as an M-K stretching vibration, where K represents the combined effects of the surrounding ions. To a first approximation, the frequency of this stretching mode depends on the square roots of the force constant of the bond and the reciprocal of the reduced mass. The force constant in turn depends on the bond length (related to the ionic radius) and covalence (related to the difference between the electronegativities of the ions) and the reduced mass (which depends on the masses of the ions) and it is affected by the properties of the nearest neighbor ions. Among the cations of interest, Mg^{2+} has the lowest mass and Fe^{2+} the heaviest, and Ca^{2+} has the largest radius. Among the bonds involved, the Si-O bond has the highest degree of covalence (~50%) and Ca-O has the lowest (~20%). The decrease of Raman shift of peak 3 with increasing molar ratio of Fe^{2+} and Ca^{2+} appears to be caused by changes in both mass and bond length brought about by the substitution in octahedral sites of the heavier cations for Mg^{2+}.

The frequency dependence of the Si-O_{nb} stretching mode (~1000 cm^{-1} in R1) and the Si-O_b-Si stretching mode (~670 cm^{-1} in R2) as functions of the molar ratios of octahedral cation (Mg^{2+}, Fe^{2+}, Ca^{2+}) reflects next nearest neighbor effects on these vibrations. In pyroxene structures, the M1 cation shares six non-bridging O atoms with $[Si_2O_6]^{4-}$ chain units and the M2 cation shares four non-bridging and two (or four) bridging O atoms with the chain units. The high covalency of the Si-O_{nb} bond in the combination Si-O_{nb}-M determines that Si-O_{nb} vibrations will be the dominant features in the Raman spectrum. The properties of the M cation will nevertheless affect the vibration frequency of the Si-O_{nb} bond. If we consider mainly the effect of mass, we can consider the combined mass of the O_{nb}-M pair as an "apparent mass" of O_{nb} in the Si-O_{nb} stretching vibration. When a heavy cation (Ca^{2+} or Fe^{2+}) is substituted for a lighter one (Mg^{2+}), this "apparent mass" of O_{nb} increases, thus increasing the reduced mass in the Si-O_{nb} stretching vibration and reducing the Raman shift of peak 1. The same argument can be made for the frequency shift of the Si-O_b-Si stretching mode (peak 2). In that case, we consider the Si-O_b-Si symmetric stretch as a mode that couples (in phase) the two Si-O_3 (O_3 is a bridging O atom) stretching modes of two $[SiO_4]^{4-}$ subunits. The substitution of a heavy cation for a lighter one in the M_2 site will increase the "apparent mass" of O_b, thus increasing the reduced mass of each Si-O_b stretching vibration, and decreasing the Raman shift of peak 2. Similar changes in Raman peak positions have also been observed in olivine (Guyot et al. 1986) and in carbonates (Bischoff et al. 1985).

Determination of pyroxene cation mole fraction using Raman data

The correlation between pyroxene composition and Raman peak positions. Given three peaks and three cations, a set of three linear equations relating them can be written and the coefficients of each equation determined from the observed dependence of peak positions on cation compositions. Using the multiple linear regression program of a statistics software package SYSTAT™ 6.0, we obtained the matrix of coefficients of the following equation:

$$n_i = a_i X^{Mg2+} + b_i X^{Fe2+} + c_i X^{Ca2+} + d_i \qquad (i = 1, 2, 3)$$

In this equation, n_i is the frequency (cm^{-1}) of the Raman peak (i), X^{Mg2+}, X^{Fe2+}, X^{Ca2+} are the molar ratios of Mg^{2+}, Fe^{2+}, and Ca^{2+} in octahedral sites, and $(X^{Mg2+} + X^{Fe2+} + X^{Ca2+}) \leq 2.0$. In principle, we can calculate the molar ratios of Mg^{2+}, Fe^{2+}, and Ca^{2+} from measured Raman peak positions of pyroxenes using the coefficients obtained. Unfortunately, because the direction of the peak shift is the same for Fe^{2+} and Ca^{2+}, these coefficients have such large uncertainties that precision in predicting cation fractions is mediocre. This occurs largely because of the nature of peak 1 in R1. As indicated by the polarized Raman measurements, the two Raman component peaks in the ~1000 cm^{-1} region have different symmetries, so the relative intensities of the two component peaks and the extent of their overlap depend on the crystal orientation relative to the laser beam, even in unpolarized beam measurements. This affects the apparent location of peak 1. In contrast, the frequencies of peaks 2 and 3 are independent of crystal orientation. Use of only two peaks limits our calibration to two cation ratios, but greatly improves precision, so this procedure is followed.

The multiple linear regression calculation was conducted to obtain the coefficients from the following equations:

$$\nu_i = a_i X^{Mg2+} + b_i X^{Ca2+} + c_i \qquad (i = 2, 3)$$

Here, ν_i is the frequency (cm^{-1}) of Raman peak 2 or peak 3, X^{Mg2+} = [moles Mg^{2+}/(moles Mg^{2+} + moles Fe^{2+} + moles Ca^{2+})] and X^{Ca2+} = [moles Ca^{2+}/(moles Mg^{2+} + moles Fe^{2+} + moles Ca^{2+})] (= Wo content). We prefer to use the ratio X^{Mg2+} instead of the more common *Mg'* = [moles Mg^{2+}/(moles Mg^{2+} + moles Fe^{2+})] in this calculation, because the frequencies of the Raman peaks correlate better with it. The coefficient matrix (a_i, b_i, c_i) is as follows, where the uncertainties are standard errors; these uncertainties are greater for the Ca^{2+} coefficients than for the Mg^{2+} coefficients:

31.9 ± 2.2 –7.7 ± 4.8 655.0 ± 1.5
51.7 ± 2.6 20.5 ± 5.9 297.3 ± 1.9

Testing the correlation on basaltic pyroxenes. We applied this correlation to the set of data from which we derived the coefficients to determine the extent of scatter about the correlation line. We also applied it to data for basaltic pyroxene grains in a thin section (no. 357 lithology B) of Martian meteorite EETA79001. For both data sets, electron microprobe analyses have been made on the same spots analyzed by Raman spectrometry. The values of X^{Mg2+} and X^{Ca2+} (=Wo) calculated from the Raman data for the 33 lunar 15273,7039 pyroxenes and the 42 Martian EETA79001,357 pyroxenes are compared with the EMP values in Figures 5a and 5b. The calculated values match the observed values to within about ± 0.1 for both X^{Mg2+} and X^{Ca2+}, and the match is equally good for both the lunar basalt data and the Martian meteorite data. The only problem with the Raman method occurs at very low mole fractions of Ca^{2+}.

The cause of the discrepancy for Ca^{2+} at low concentrations arises because, as pointed out above, Raman peak position is more sensitive to Mg^{2+} molar fraction than to Ca^{2+}. The multiple linear regression calculation reveals that some 80–90% of peak shift of Raman peaks 2 and 3 is caused by the variation of X^{Mg2+}. Substitutions of both Ca^{2+} and Fe^{2+} for Mg^{2+} move peak positions to lower Raman shifts, and most pyroxenes with low Ca^{2+} have much more Fe^{2+} than Ca^{2+}, so the effect of small amounts of Ca^{2+} is difficult to discern. Large relative errors for calculated X^{Ca2+} values thus occur for orthopyroxenes at values of X^{Ca2+} <0.07 (Fig. 6a). These large errors can result in values for X^{Ca2+} of 0.1–0.2 for cases in which X^{Ca2+} is actually ≤0.1. These errors occur only for orthopyroxene and they occur for all orthopyroxenes, however, so they are readily discovered

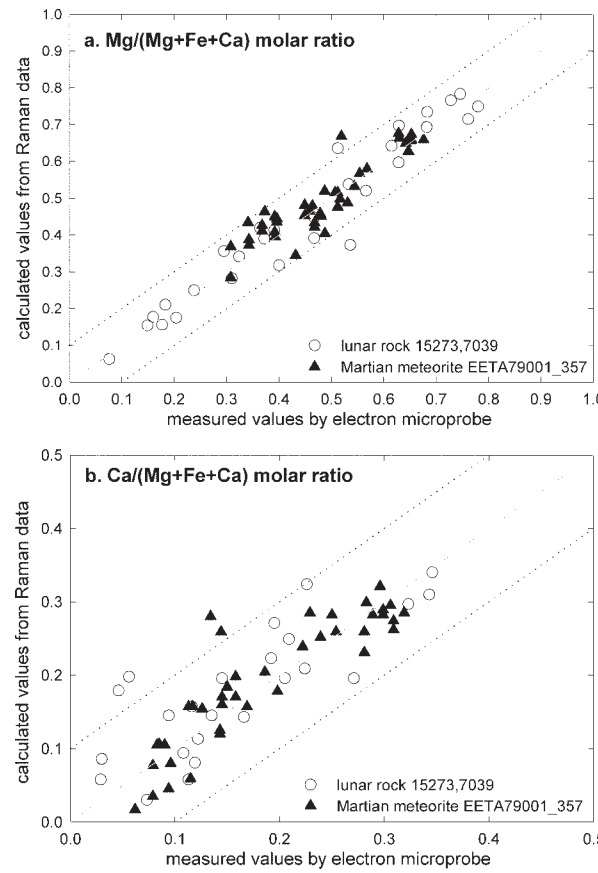

FIGURE 5. Values obtained from Raman measurements are compared with EMP-determined values of cation mole fraction for basaltic pyroxenes in a Martian meteorite and in the lunar rock used to calibrate the Raman peak positions.

and rectified once the orthopyroxene has been identified from its spectral pattern (Fig. 3). The large relative errors in X^{Ca2+} that occur at low Ca^{2+} concentrations do not affect the accuracy of calculated values of X^{Mg2+} (Fig. 6b) because the Ca^{2+} concentrations are so low. In summary, values of X^{Mg2+} and X^{Ca2+} can be measured by Raman spectroscopy with an accuracy of ±0.1 units.

There are four main reasons why Raman-derived values of cation fraction do not agree even more precisely with the values obtained by EMP analysis: coregistration of the instrument beams onto the same point, particularly in strongly zoned pyroxenes; differences in the volume sampled between the two instruments; uncertainty in Raman peak positions; and the presence of minor cations (Al^{3+}, Ti^{4+}, Cr^{3+}, Na^{+}) in the pyroxene structure, which affect Raman peak positions. This last effect was ignored in the development of the coefficient matrix. Particular care was taken to remove any error in coregistration of the locations for 10 spots on thin section no. 357 of EETA79001 where the Raman and EMP data were taken. For this, we measured distances to the sampling spot from unmistakable points on the thin section, resulting in errors in location of less than 10 μm. The reduction in errors of location did not greatly improve the agreement between the values of cation fraction calculated from the Raman data and the values derived from the EMP measurements. Precise coregistration of the sampling points does not correspond to sampling of the same volume of the mineral grain by both methods. The Raman instrument samples deeper (a few micrometers to millimeters, except in very dark materials such as graphite, Haskin et al. 1997) than the electron microprobe (≤1 μm at the beam currents we use; Goldstein et al. 1981) and, depending on the mineral grain and its enclosing matrix, the Raman instrument may sample a wider volume.

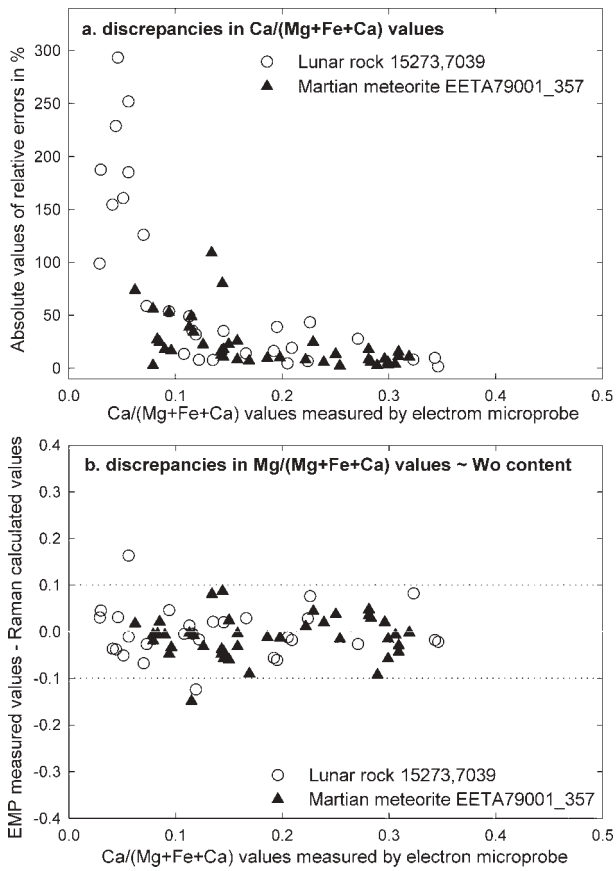

FIGURE 6. Absolute values of discrepancies between values derived from Raman measurements and those by EMP analyses are shown for basaltic pyroxenes as a function of cation mole fraction. Note the large percent errors for Ca^{2+} mole fraction at values <0.07. These erroneous values are all overestimates and can be detected and corrected because the structural pattern of the spectra allows their identification as low-Ca orthopyroxene.

Testing the correlation on well equilibrated pyroxenes. Does the correlation between Raman peak positions and pyroxene compositions also hold for well equilibrated pyroxenes? As a test, we measured the Raman spectra of several sets of well equilibrated pyroxene samples. Compositional data for these pyroxenes were available from EMP analyses, but not taken on the same sampling spots where the Raman analyses were done, and in some cases, only on samples from the same locality (Table 1). The equilibrated samples include three sets of lunar pyroxene samples and five sets of terrestrial pyroxenes, 122 data points in all (Table 1).

Values of X^{Mg2+} calculated from the Raman data are compared with those obtained by EMP analysis in Figure 7a. The discrepancies for all but three data points are smaller than ±0.1, surprisingly good considering that these EMP and Raman analyses were not all taken on the same sampling spots. This shows that values of X^{Mg2+} of well-equilibrated pyroxenes can readily be derived from the Raman data using the same correlation as for basaltic pyroxenes and with similar accuracy.

Unfortunately, this is not the case for X^{Ca2+}. Compared to basaltic pyroxenes, discrepancies between Raman-derived and EMP measured values for X^{Ca2+} for the well-equilibrated pyroxenes are large in some cases (Fig. 7b). In some cases of low-Ca pyroxene, values of X^{Ca2+} calculated from the peak positions are too high; in other cases, they are too low. We get the most reliable information about X^{Ca2+} by careful analysis of the spectral pattern. As in the case of the basaltic pyroxenes, if the spectral pattern is that of orthopyroxene, then we know that high values of X^{Ca2+} calculated from Raman peak positions are incorrect, and the true values are <0.1. In some cases of high-Ca pyroxene, the value of X^{Ca2+} based on Raman peak positions was found to be too low. The spectral pattern in these cases is that of monoclinic pyroxene. The most extreme example of this is hedenbergite (QUE94281, Fig.7b), but because of the unique spectral pattern of hedenbergite (Fig. 1e), we can recognize the error and know that X^{Ca2+} is in the range ~0.35 – 0.5. In other cases, we only know the sum of X^{Ca2+} and X^{Fe2+} from the value of X^{Mg2+}.

Compared with basaltic pyroxenes, the generally larger discrepancies between the calculated and measured X^{Ca2+} for well-equilibrated pyroxenes may reflect the preferred occupancy by Ca^{2+} of M2 sites. One would expect an ordered cation distribution in well-equilibrated pyroxenes to affect Raman peak posi-

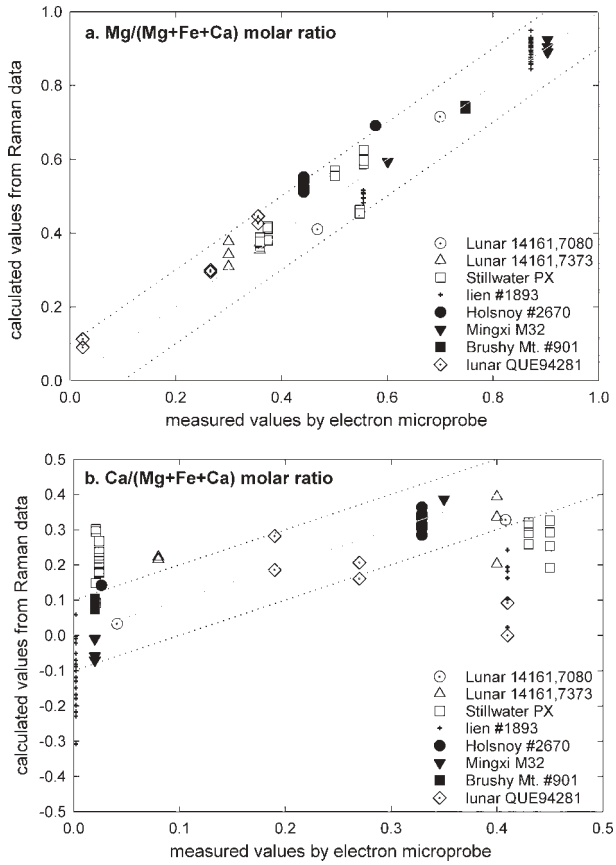

FIGURE 7. Predicted values obtained from Raman measurements are compared with EMP-determined values of cation mole fraction for equilibrated pyroxenes in two lunar rocks and five terrestrial samples. Errors for Mg^{2+} cation fraction are of the same magnitude as for basaltic pyroxenes (~0.1). The larger errors for both low-Ca orthopyroxene and hedenbergitic high-Ca pyroxenes can be detected from the structural patterns and corrections made.

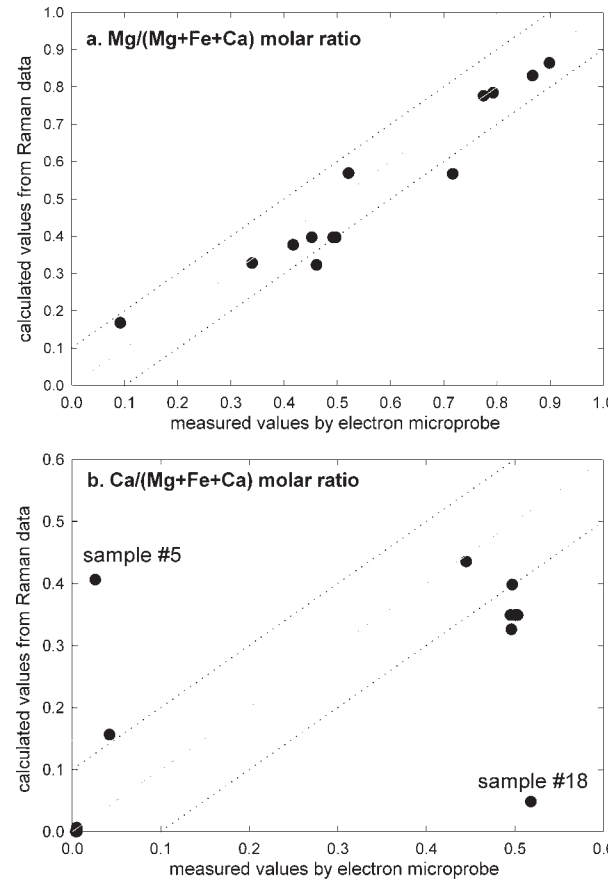

FIGURE 8. Values of cation molar fraction calculated using the Raman data of Huang et al. (2000) of 13 natural pyroxenes are compared with the values derived from their EMP data.

tions in a manner different from the quasi-random distribution in rapidly cooled basaltic pyroxenes.

We have used the above correlations to calculate the cation molar ratios of 13 natural pyroxene samples reported in the study of Huang et al. (2000). Except in two cases, we found good agreement between the X^{Mg2+} and X^{Ca2+} calculated from our equations using their Raman data and the values calculated from their EMP data (Fig. 8). Among these data, only two X^{Mg2+} values have discrepancies slightly beyond ±0.1. Discrepancies of X^{Ca2+} values are somewhat greater, as we also found among our samples. A large X^{Ca2+} discrepancy is found for sample no. 5 (Fig. 8, based on the correlation between peaks 2 and 3). Use of our less precise estimate on the basis of peaks 1 and 3 gives values of X^{Mg2+} = 0.8 and X^{Ca2+} = 0, which are within ±0.1 of those derived from the EMP data (X^{Mg2+} = 0.72 and X^{Ca2+} = 0.03). The reason for the anomalous value based on peaks 2 and 3 is unknown. Another outlier is a hedenbergite (sample no. 18). The Raman data give a good estimate of X^{Mg2+}, but a low estimate of X^{Ca2+}; this can be corrected by taking into account the characteristic spectral pattern.

Determining characteristics of pyroxene in rocks by remote "point counting" Raman measurements

In the preceding sections, we showed how Raman spectral patterns could be used to determine pyroxene structural types and we used Raman data and EMP data to calibrate Raman peak positions for pyroxene cation composition. In this section, we apply this information to Raman point-counting data, i.e., data obtained by scanning across sample surfaces and taking Raman spectra at fixed intervals without focusing the beam on the individual points (Haskin et al. 1997). The quality of the data, especially on rough, unprepared surfaces, is not as high as that of the data used in the previous sections of the paper. These data, however, are comparable to what would be obtained in the field or on the surface of another planet.

We obtained three sets of remote "point counting" Raman measurements on three rocks of different types of sample surfaces: two rastering scans (rectangular grids) over a few pyroxene grains on the smooth surface of a thin section of Stillwater rock (S2-123); three linear traverses and two rastering

scans on a flat-cut, unpolished surface of Martian meteorite Zagami; and four linear traverses on a rough broken surface of rock chip no. 476 of Martian meteorite EETA79001, lithology A (Table 1).

The issue of interest in these experiments is how well we can characterize the pyroxene in these rocks from such data. It is convenient for this purpose to plot the shifts of Raman peaks 2 and 3 against each other to get an overview of the spread in X^{Mg2+} for a set of pyroxene grains from a single sample. Figure 9a is a diagram of this type that includes the pyroxene data from the calibration rock, lunar sample 15273,7039 (open circles). These data spread in a continuous way and cover a wide range of X^{Mg2+}, from 0.1 to 0.8. This distribution reflects a continuous variation of X^{Mg2+} values among or within these pyroxene grains. This indicates a rapid cooling process in which equilibrium was not maintained between the pyroxene and its crystallizing contemporary melt and that no exsolution occurred during cooling. The two-peak plot (Fig. 9a) provides a simple way to distinguish basaltic pyroxene from well-equilibrated pyroxene, as shown below. Similarly, continuous data distributions are observed for Martian meteorite pyroxene in Zagami (Fig. 3 in Wang et al. 1999) and in EETA79001 lithology A (Fig. 9a), which also reflects their basaltic textures.

The 58 Raman spectra of pyroxene obtained from the thin section of Stillwater sample S2-123 can be divided into three groups. Fifty show a spectral pattern typical of orthorhombic pyroxene, with a doublet in spectral region R2 (~673 cm^{-1} for high frequency peak) and high Raman shifts for all other peaks.

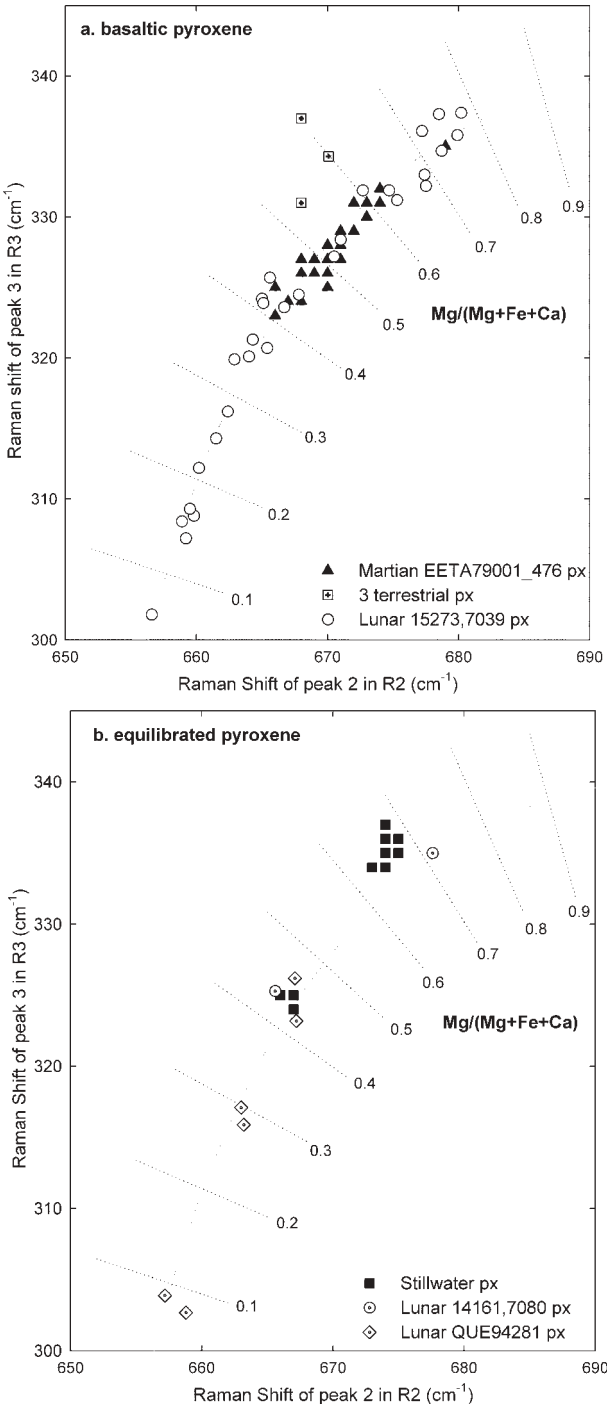

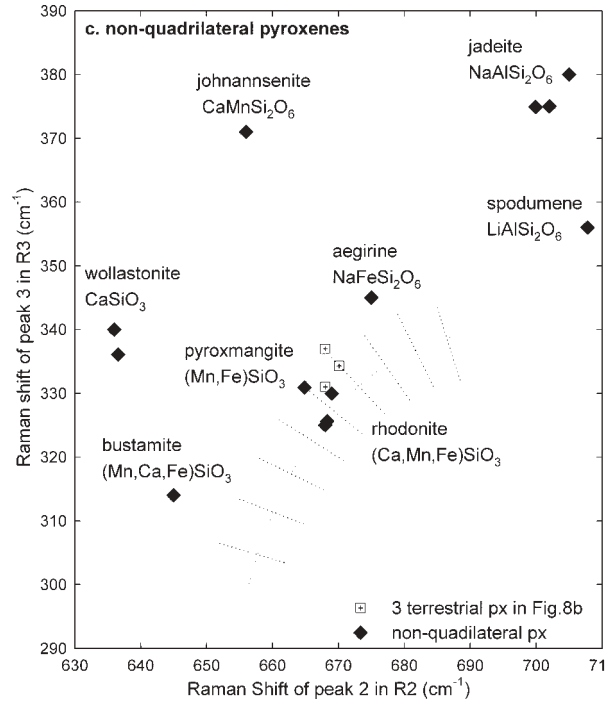

FIGURE 9. The monotonic change in position of Raman peak 3 relative to peak 2 is shown. The central dashed line in a and b is the combined result from the regressions of the positions of peaks 2 and 3 against X^{Mg2+} [Mg/(Mg + Fe + Ca)] for the Raman and EMPA data of pyroxene from lunar sample 15273,7039. Peak positions of orthorhombic pyroxene plot at the highest values of Mg^{2+} cation fraction and peak positions of triclinic pyroxenoid plot at the lowest values. The dashed lines perpendicular to the central line separate regions of different X^{Mg2+}. The gap between points for the equilibrated pyroxene in b indicates the presence of a host pyroxene and exsolution lamellae and identifies the pyroxene as equilibrated. Part c contains the same correlation curve, but on a smaller scale, and shows that non-quadrilateral pyroxene can deviate strongly from the calibration for quadrilateral pyroxene.

Three spectra show a typical spectral pattern of monoclinic pyroxene, having a single peak in R2 (~664 cm^{-1}). The third type of spectrum has a pattern that is a mixture of the other two patterns, suggesting the measurement spots covered both orthorhombic and monoclinic pyroxenes. The data for the Stillwater pyroxenes (Fig. 9b) lie along the calibration curve determined from the lunar basaltic pyroxenes, indicating that the correlation between the positions of Raman peak 2 and peak 3 is very similar for both basaltic and equilibrated quadrilateral pyroxenes. In other words, this correlation is not severely affected by the ordered distribution of Ca^{2+} cations in equilibrated quadrilateral pyroxenes. The Stillwater data in Figure 9b are clearly separated into a bimodal distribution. This distribution indicates the presence of slowly cooled pyroxene with well developed exsolution lamellae, in which orthorhombic pyroxene is the host and the exsolved lamellae are monoclinic pyroxene. The data from two other sets of equilibrated quadrilateral pyroxene from lunar samples 14161,7080 and QUE94281 (Fig. 9b) also separate into clusters and lie along the calibration curve.

For pyroxene varieties that have high concentrations of non-quadrilateral components (e.g., Al, Na, Li), the correlation of positions of the two Raman peaks is affected. Three data points in Figure 9a are from terrestrial pyroxene samples that have high concentrations of non-quadrilateral components (~8.03–8.73 wt% Al_2O_3, ~0.84–1.27 wt% Cr_2O_3, ~0.82–0.87 wt% Na_2O). The locations of these data points in Figure 9a are shifted away from the correlation line. Figure 9c shows the Raman data of a few non-quadrilateral pyroxenes. The differences in correlation of peak positions for the non-quadrilateral pyroxenes are obvious. Also, non-quadrilateral pyroxenes and pyroxenoids have significantly different Raman spectral patterns (Fig. 10) resulting from large differences either in cation properties or in silicate chain structures

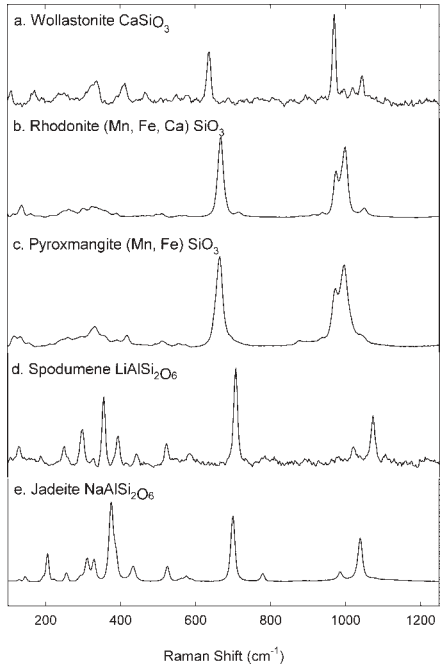

FIGURE 10. Raman spectra are show for several non-quadrilateral pyroxenes.

The "point counting" Raman measurements on Martian meteorites Zagami and EETA79001 lithology A produced over seven hundred pyroxene spectra. These data are summarized in two histograms (Figs. 11a and 11b) of the position of Raman peak 3, because peak 3 has the tightest linear correlation with X^{Mg2+}. The data from point counting measurements on two lunar samples (a rock chip of 15273,7039 and a thin section of 14161,7062) and on two terrestrial samples (a thin section of Stillwater anorthosite S2-123 and a rock chip of a Lien garnet pyroxenite no. 1893) are also shown in Figure 11 for comparison. The histograms of lunar and terrestrial pyroxenes (Figs. 11c–f) show that we can determine whether pyroxene cooled rapidly as in a basalt or cooled slowly with exsolution with as few as 20–50 spectral data points. For basaltic pyroxene in

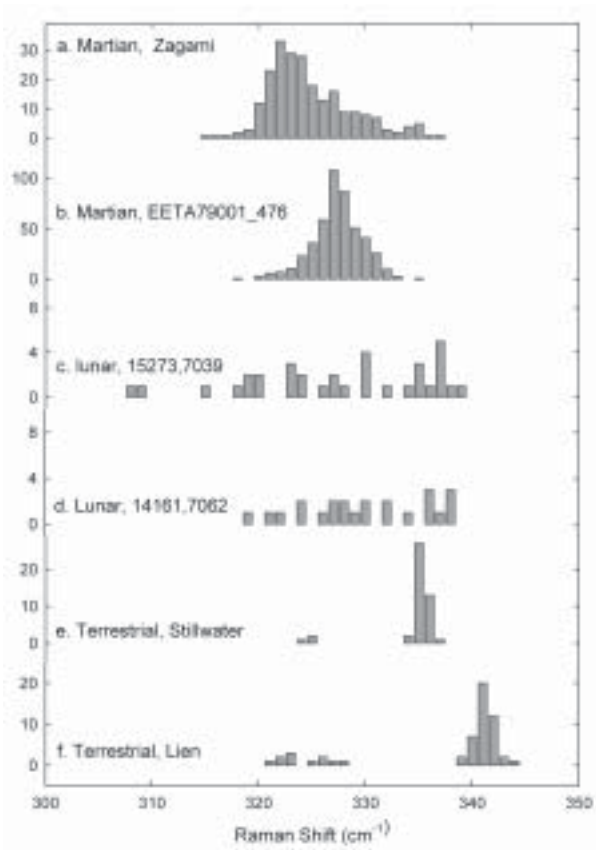

FIGURE 11. Frequency distributions of peaks in the 300–400 cm^{-1} region (peak 3) obtained by point-counting Raman experiments are shown for pyroxenes from different rock types. The continuous distributions for the Zagami meteorite in **a** (229 spectra) is slightly bimodal, consistent with the presence of phenocrysts (known to be present also from the constant peak positions of several sets of adjacent counting points). That for EETA 79001 in **b** (476 spectra) is typical of basaltic texture in which cooling was rapid. The distributions for the Stillwater anorthosite **e** (46 spectra) and Lien pyroxenite **f** (55 spectra) are characteristic of equilibrated orthopyroxene with exsolved clinopyroxene. The broad range and relatively flat distributions in KREEP basalts in **c** and **d** are not from point counts but from points selected on the basis of petrography to provide the compositional spread necessary to develop the calibration.

TABLE 4. Ranges of Mg/(Mg+Fe+Ca) and Ca/(Mg+Fe+Ca) values derived from Raman point-counting measurements from three rocks

Stillwater rock		EETA79001-A meteorite		Zagami meteorite	
Mg/(Mg+Fe+Ca)	Ca/(Ca+Fe+Mg)	Mg/(Mg+Fe+Ca)	Ca/(Ca+Fe+Mg)	Mg/(Mg+Fe+Ca)	Ca/(Ca+Fe+Mg)
Calculated values based on Raman point-counting data					
0.57–0.62 (opx)	0.17–0.30* (opx)	0.27–0.74	0.0–0.37	0.23–0.68	0.01–0.48
0.36–0.38 (cpx)	0.26–0.34* (cpx)				
EMPA data† from literature or EMPA on different grains					
0.55–0.56 (opx)	0.02 (opx)	0.38–0.70	0.06–0.31	0.33–0.61	0.08–0.32
0.37 (cpx)	0.45 (cpx)				

* The spectral pattern of these pyroxenes indicate that they have orthorhombic structure; this information is used to correct the Ca/(Mg+Fe+Ca) calculation error associated with equilibrated pyroxene (see discussion in text).
† Data from McSween and Jarosewich (1983), Stolper & McSween (1979), and Brearley (1991) for EETA79001 and Zagami; and our analyses of the Stillwater sample.

Zagami and EETA79001 lithology A, the large number of Raman point-counting data provides additional information from the peak shape of the histogram (Figs. 11a and 11b). The peak in the EETA79001-A histogram is Gaussian with a width that somewhat exceeds that from measurement uncertainty. This Gaussian peak shape suggests a single-stage cooling process. In contrast, the histogram of Zagami pyroxenes is broader and asymmetric. It can be deconvolved into two overlapping Gaussian components. This feature indicates that the crystallization history of Zagami pyroxenes is thus more complicated.

The distributions of X^{Ca2+} and X^{Mg2+} for the pyroxenes in three rock samples (Stillwater anorthosite and the Martian meteorites Zagami and EET79001–A) as calculated on the basis of Raman point-counting data, are listed in Table 4. The distribution of values obtained in this manner can be compared with the distribution of the published pyroxene compositions for these rocks. Our Raman-derived values cover a larger compositional range than the published EMPA data for EETA79001 and Zagami (McSween and Jarosewich, 1983; Stolper and McSween, 1979; Brearley 1991). The differences, however, are within ±0.1 unit for both X^{Mg2+} and X^{Ca2+} values. Given that the EMPA and Raman data were not obtained from the same samples, let alone the same points, and that EMPA measurements are normally taken at selected spots and would not necessarily cover the same range, these differences indicate acceptable agreement. Similarly, the X^{Mg2+} values derived from Raman data for both orthopyroxene and clinopyroxene in the sample of Stillwater anorthosite are in good agreement with the EMPA data analyzed on the same sample but different grains. The Raman data for X^{Ca2+} values, taken at face value, are too high in some cases, as observed for some other equilibrated pyroxenes. As pointed out, however, X^{Ca2+} values should not be taken at face value, but based on the type of pyroxene (also determined from the Raman spectra), overestimated values of X^{Ca2+} can be detected and corrected.

In summary, the major structural and compositional features of quadrilateral pyroxenes can be determined using Raman spectral pattern characteristics and the correlation calculation based on major Raman peak positions. The correlated variation in Raman peak position also helps to distinguish non-quadrilateral pyroxene (or quadrilateral pyroxene enriched with non-quadrilateral components) from quadrilateral pyroxene. Furthermore, the Raman data from point counting procedures on rock samples, although low in S/N ratio, are sufficient to characterize the major chemical features of the pyroxene in these rock samples and thus help us to understand the conditions of formation and the history of pyroxene crystallization in rocks.

ACKNOWLEDGMENTS

This work was supported in part by NASA grant NAG5-7140. We are grateful to E. Huang and an anonymous reviewer for their constructive comments, which helped us improve the manuscript.

REFERENCES CITED

Armstrong, J.T. (1988) Quantitative analysis of silicate and oxide minerals: Comparison of Monte-Carlo, ZAF, and phi-rho-Z procedures. Microbeam Analysis, 239–246.

Bilton, M.S., Gilson, T.R., and Webster, M. (1972) The vibrational spectra of some chain type silicate minerals. Acta, 28A, 2113–2119.

Bischoff, W.D., Sharma, S.K., and Mackenzie, F.T. (1985) Carbonate ion disorder in synthetic and biogenic magnesian calcites: a Raman spectral study. American Mineralogist, 70, 581–589.

Brearley, A.J., (1991) Subsolidus microstructures and cooling history of pyroxenes in the Zagami shergottite. Lunar and Planetary Science XXII, 135–136.

Brown, G.M. (1972) Pigeonitic pyroxenes: A review. Geological Society of America Memoir, 132, 523–534.

Burnham, C.W. (1971) The crystal structure of pyroxferroite from Mare Tranquillitatis. Proceedings of the Second Lunar Science Conference, 47–57.

Christensen, P.R., Bandfield, J.L., Smith, M.D., Hamilton, V.E., and Clark, R.N. (2000) Identification of a basaltic component on the Martian surface from Thermal Emission Spectrometer data. Journal of Geophysical Research, 105, 9609–9621.

Deer, W.A., Howie, R.A., and Zussman, J. (1997) Magnesium-Iron Pyroxenes. In Rock-forming minerals, vol. 2A: The single chain silicates (2nd ed.), p. 20–34. Alden Press, Oxford.

Dele-Dubois, M.L., Dhamelincourt, P., and Schubnel, H.J. (1980) Etude par spectroscopie Raman d'inclusions dans les diamants, saphirs et emeraudes/2. Revue de Gemmologie A.F.G., 64, 11–14.

Edwards, H.G.M., Farwell, D.W., Grady, M.M., Wynn-Williams, D.D., and Wright, I.P. (1999) Comparative Raman spectroscopy of a Martian meteorite and Antarctic lithic analogues. Planetary and Space Science, 47, 353–362.

Etchepare, J. (1970) Study by Raman spectroscopy of crystalline and glassy diopside. In R.W. Douglas and B. Ellis, Eds., Amorphous materials, p. 337–346. Wiley, New York.

Fabel, G.W., White, W.B., White, E.W., and Roy, R. (1972) Structure of lunar glasses by Raman and soft X-ray spectroscopy. Proceeding of the Third Lunar Science Conference, Geochimica et Cosmochimica Acta (suppl.), 1, 935–951.

Ghose, S., Choudhury, N., Chaplot, S.L., Chowdhury, C.P., and Sharma, S.K. (1994) Lattice dynamics and Raman spectroscopy of protoenstatite $Mg_2Si_2O_6$. Physics and Chemistry of Minerals, 20, 469–477.

Goldstein, J.I., Newbury, D.E., Echlin, P., Joy, D.C., Fiori, C., and Lifshin, E. (1981) Scanning Electron Microscopy and X-Ray Microanalysis, 673 p. Plenum Press, New York.

Guyot, F., Boyer, H., Madon, M., Velde, B., and Poirier, J.P. (1986) Comparison of the Raman microprobe spectra of $(Mg,Fe)_2SiO_4$ and Mg_2GeO_4 with olivine and spinel structures. Physics and Chemistry of Minerals, 13, 91–95.

Haskin, L.A. and Salpas, P.A. (1992) Genesis of compositional characteristics of Stillwater AN-I and AN-II thick anorthosite units. Geochimica et Cosmochimica Acta, 56, 1187–1212.

Haskin, L.A., Wang, A., Rockow, K.M., Jolliff, B.L., Korotev, R.L., and Viskupic, K.M. (1997) Raman spectroscopy for mineral identification and quantification for in situ planetary surface analysis: A point count method. Journal of Geophysical Research, 102, 19293–19306.

Haskin, L.A., Wang, A., Jolliff, B.L., Wdowiak, T., Agresti, D., Lane, A. L., Squyres, S. (2001) The Mars Microbeam Raman Spectrometer (MMRS), abstract no. 1705, Lunar and Plantery Science XXXII, Lunar and Planetary Institute, Houston.

Huang, E., Chen, C.H., Lin, E.H., and Xu, Ji-an (2000) Raman spectroscopic characteristics of Mg-Fe-Ca pyroxenes. American Mineralogist, 85, 473–479.

Jolliff, B.L. (1994) Searching for rare highland igneous rocks at Apollo 14: Fragments of magnesian-suite assemblages. Lunar and Planetary Science XXV, 633–634.

Jolliff, B.L., Korotev, R.L., and Haskin, L.A. (1991) Geochemistry of 2–4 mm particles from Apollo 14 soil (14161) and implications regarding igneous components and soil-forming processes. Lunar and Planetary Science XXI, 193–219.
Jolliff, B.L., Rockow, K.M., and Korotev, R.L. (1998) QUE94281 lunar meteorite: Petrology and geochemistry of very-low-Ti mafic components and highland components. Meteoritics and Planetary Science, 33, 581–601.
Jolliff, B.L., Floss, C., McCallum, I.S., and Schwartz, J.M. (1999) Geochemistry, petrology, and cooling history of 14161,7373: A plutonic lunar sample with textural evidence of granitic-fraction separation by silicate-liquid immiscibility. American Mineralogist, 84, 821–837.
McSween, H.Y. Jr. (1994) What have we learned about Mars from SNC meteorites? Meteoritics, 29, 757–779.
McSween, H.Y. Jr. and Jarosewich, E. (1983) Petrogenesis of the Elephant Moraine A79001 meteorite: Multiple magma pulses on the shergottite parent body. Geochimica et Cosmochimica Acta, 47, 1501–1513.
Meyer, C. (1996) Mars Meteorite Compendium—1996. JSC Report no. 27672, p. 43–50, 67–90. Johnson Space Center, Houston.
Ohashi, H. and Sekita, M. (1982) Raman spectroscopic study of the Si-O-Si stretching vibration in clinopyroxenes. Journal of the Japanese Association of Mineralogists, Petrologists and Economic Geologists, 77, 455–459.
———(1983) Raman spectroscopic study of clinopyroxenes in the join $CaScAlSiO_6$-$CaTiAl_2O_6$. Journal of the Japanese Association of Mineralogists, Petrologists and Economic Geologists, 78, 239–245.
Ohashi, Y. and Finger, L.W. (1975) Pyroxenoids; a comparison of refined structures of rhodonite and pyroxmangite. Yearbook, Carnegie Institution of Washington, 74, 564–569.
Papike, J.J. (1996) Pyroxene as a recorder of cumulate formational processes in asteroids, Moon, Mars, Earth: Reading the record with the ion microprobe. American Mineralogist, 81, 525–544.
Papike, J.J. and Cameron, M. (1976) Crystal chemistry of silicate minerals of geophysical interest. Reviews of Geophysics and Space Physics, 14, 37–80.
Papike, J.J., Prewitt, C.T., Sueno, S., and Cameron, C. (1973) Pyroxenes: comparisons of real and ideal structural topologies. Zeitschrift für Kristallographie, 138, 254–273.
Perry, C.H., Agrawal, D.K., Anastassakis, E., Lowndes, R.P., and Tornberg, N.E. (1972) Far infrared and Raman spectroscopic investigations of lunar materials from Apollo 11, 12, 14, and 15. Proceeding of the Third Lunar Science Conference, Geochimica et Cosmochimica Acta (suppl.), 3, 3077–3095.
Rutstein, M.S., and White, W.B. (1971) Vibrational spectra of high calcium pyroxenes and pyroxenoids. American Mineralogist, 56, 877–887.
Sekita, M., Ohashi, H., and Terada, S. (1988) Raman study of clinopyroxene in the system $CaScAlSiO_6$–$CaAl_2SiO_6$($CaScAlSiO_6$-$CaTiAl_2O_6$). Physics and Chemistry of Minerals, 15, 319–322.
Sharma, S.K., Simons, B., and Yoder, H. Jr. (1983) Raman study of anorthite, calcium Tschermak's pyroxene, and gehlenite in crystalline and glassy states. American Mineralogist, 68, 1113–1125.
Sharma, S.K. and Simons, B. (1981) Raman study of crystalline polymorphs and glasses of spodumene composition quenched from various pressures. American Mineralogist, 66, 118–126.
Sharma, S.K., Virgo, D., and Mysen, B.O. (1979) Raman study of the coordination of aluminum in jadeite melts as a function of pressure. American Mineralogist, 64, 779–787.
Smyth, J.R., and Bish, D.L., (1988) Crystal structures and cation sites of the rock-forming minerals, p. 156–166. Allen and Unwin Inc., Boston.
Stolper, E.M. and McSween, H.Y. Jr. (1979) Petrology and origin of the Shergottite meteorites. Geochimica et Cosmochimica Acta, 43, 1475–1498.
Wang, A., Jolliff, B.L., and Haskin, L.A. (1995) Raman spectroscopy as a method for mineral identification on lunar robotic exploration missions. Journal of Geophysical Research, 100, 21189–21199.
Wang, A., Jolliff, B.L., Viskupic, K.M., and Haskin, L.A. (1997) Raman spectroscopic characterization of different types of pyroxene. Lunar and Planetary Science XXVIII, 1491–1492.
Wang, A., Haskin, L.A., and Cortez, E. (1998) A Raman spectroscopic sensor for in situ mineral characterization on planetary surfaces. Applied Spectroscopy, 52, 477–487.
Wang, A., Jolliff, B.L., and Haskin, L.A. (1999) Raman spectroscopic characterization of a Martian SNC meteorite: Zagami. Journal of Geophysical Research, 104, 8509–8519.
Wang, A., Haskin, L.A., Kuebler, K.E., Jolliff, B.L., and Walsh, M.M. (2001) Raman spectroscopic detection of graphitic carbon of biogenic parentage in an ancient South African chert, no. 1423, Lunar and Planetary Science XXXII.
Wdowiak, T.J., Agresti, D.G., Mirov, S.B., Kudryavtsev, A.B., and Beele, L.W. (1997) Identification of ancient carbonaceous cherts on Mars using Raman spectroscopy, Conference on Early Mars, Houston.
White, W.B. (1975) Structural interpretation of lunar and terrestrial minerals by Raman spectroscopy. In C. Karr, Jr., Ed., Infrared and Raman spectroscopy of Lunar and terrestrial minerals, p. 325–358. Academic Press, New York.
Wynn-Williams, D.D. and Edwards, H.G.M. (2000) Proximal analysis of regolith habitats and protective biomolecules in situ by Laser Raman spectroscopy: Overview of terrestrial Antarctic habitats and Mars analogs. Icarus, 144, 486–503.

MANUSCRIPT RECEIVED OCTOBER 10, 2000
MANUSCRIPT ACCEPTED MARCH 23, 2001
MANUSCRIPT HANDLED BY THOMAS DUFFY

APPENDIX: SAMPLE AND RAMAN EXPERIMENTS DESCRIPTIONS

Lunar Samples

Lunar sample 15273,7039 is a 32 mg KREEP basalt fragment from a regolith sample at station 6, Apollo 15. It has an intergranular texture wherein plagioclase forms mostly long (millimeter size and smaller), slender laths and a few blocky masses (Haskin et al. 1997). Pyroxene, cristobalite, and mesostasis fill the interstices within the plagioclase mesh. Pyroxene grains, typically 0.2–0.5 mm, are compositionally zoned and include magnesian orthopyroxene, pigeonite, and augite. Some pyroxene grains zone to ferroaugite and some have thin rims or late growth zones of pyroxferroite. Analysis of pyroxene grains by EMPA reveals a range of compositions from *Mg*' [Mg/(Mg + Fe) atomic] ~0.8 (orthopyroxene cores) through intermediate *Mg*' (pigeonite and augite) to *Mg*' <0.1 (pyroxferroite) (Table 2). Thirty-five spots in zoned pyroxene grains in sample 15273,7039 were analyzed using both micro-Raman spectroscopy and EMPA. These form the set of calibration data that we used initially to establish the correlation between Raman peak positions and the major composition of quadrilateral pyroxenes.

Lunar sample 14161,7062 is a 26 mg rock fragment of a clast-free, KREEPy impact-melt rock from the Apollo 14 site (Jolliff et al. 1991; Haskin et al. 1997). It has a relatively coarse-grained intergranular texture, with plagioclase laths and masses of 1–2 mm size and interstitial pyroxene grains typically 0.3–0.5 mm. Pyroxene *Mg*' values range from 0.82 to 0.05 and Wo contents range from 3 to 32 (Table 2).

Lunar sample 14161,7080 is a 15.6 mg rock fragment that has a noritic mineral assemblage (Jolliff 1994). About 50% of the assemblage is low-Ca pyroxene of *Mg*' = 0.73, occurring in masses ranging to ~0.8 mm. Minor high-Ca pyroxene has *Mg*' = 0.79 and Wo = 41 (Table 2). The pyroxene grains are compositionally uniform, but not exsolved. This sample was strongly shocked, resulting in pervasive fracturing of pyroxene grains and conversion of plagioclase entirely to maskelynite.

Lunar sample 14161,7373 is a small rock fragment, original mass of 18.4 mg, that has an assemblage corresponding to whitlockite (REE-merrillite) monzogabbro (Jolliff et al. 1999). It contains abundant exsolved pigeonite grains, some in excess of 0.5 mm, with exsolution lamellae of augite typically ~10 μm wide. Augite grains contain fine (~5 μm) exsolution lamellae of pigeonite. Shock deformation caused pervasive fracturing but no amorphization of pyroxene or feldspar. Pyroxene compositions are fairly uniform, with pigeonite of *Mg*' ~ 0.39 and Wo ~ 7–8, and augite of *Mg*' ~ 0.50 and Wo ~ 40 (Table 2).

QUE94281 lunar meteorite was collected in Antarctica and consists of a mixed mare-basalt and highland regolith breccia (Jolliff et al. 1998). It contains abundant clasts of pyroxene ranging up to 0.8 mm, with most consisting of finely exsolved pigeonite or ferroaugite, but also including several grains of hedenbergite. Pyroxene exsolution lamellae are typically 1–2 μm or less and are difficult to avoid in microprobe analyses. Individual clasts are strongly shocked and some clasts that have pyroxene compositions are amorphous.

Martian (shergottite) meteorites

Zagami. Most of Zagami, as well as the fragment we analyzed, consists of the "normal Zagami" lithology, which is pyroxene-rich and has a diabasic or subophitic texture similar to that of the Martian meteorite Shergotty (Stolper and McSween 1979). Zagami typically exhibits a foliated texture consisting of aligned pyroxene grains and maskelynite (Stolper and McSween 1979), with maskelynite generally occupying interstices between pyroxene grains. The sample that we analyzed is a 2.5 g, flat, rectangular sawn chip measuring roughly 1.5 × 1.0 × 0.5 cm (Wang et al. 1999). A few pyroxene grains are 3–4 mm in length and 0.3–0.4 mm across, but most grains are 0.2–0.5 mm wide.

EETA79001 is generally basaltic, but very pyroxene-rich and consists mostly of two related igneous lithologies (designated A and B) separated by an igneous or impact-melt contact (McSween and Jarosewich 1983; Mittlefehldt et al. 1997). The two lithologies are related, but differ texturally and in their mineral assemblages and compositions. Pigeonite, augite, and maskelynite are the major minerals in both lithologies, but lithology A contains coarse xenocrysts or xenoliths of olivine and orthopyroxene that are somewhat more magnesian than the finer grained basaltic matrix. The groundmass of Lithology A has an average grain size of ~0.15 mm and no preferred orientation (McSween and Jarosewich 1983). Lithology B is mineralogically similar to the groundmass of A, but is coarser (mean grain size ~0.35 mm) and represents a more differentiated composition (e.g., pyroxene compositions are more extensively zoned to high-Fe concentrations [McSween and Jarosewich 1983]).

Terrestrial samples

Sample S2-123 is from a thick anorthosite unit (AN-II) of the Middle-Banded Series of the Stillwater complex (Haskin and Salpas 1992). Low-Ca and high-Ca pyroxenes occur within the anorthosite as widely distributed, coarsely exsolved grains, some forming oikocrysts up to several cm across. Oikocrysts are zoned, e.g., Mg/(Mg + Fe) ~ 0.6–0.7, but on the scale of a thin section, and aside from exsolution, individual pyroxene masses are compositionally uniform. Our analyses are of an inverted pigeonite host and augite exsolution lamellae ~15 μm wide and spaced 60–70 μm apart.

Sample 1893 is a garnet pyroxenite from Lien, Norway. The sample contains coarse orthopyroxene, clinopyroxene, and garnet (up to 2 mm) set in a fine- to medium-grained matrix of orthopyroxene, clinopyroxene, pargasitic amphibole, garnet, and spinel (Medaris 1980). Coarse pyroxene grains are zoned, with cores enriched in Al, Cr, and Na, and rim compositions approaching that of the matrix pyroxene. Orthopyroxene compositions are $En_{87.0–91.8}$ and $Wo_{0.2–0.5}$. Clinopyroxene is chromian diopside whose jadeite component [$Na(Al,Fe^{3+})Si_2O_6$] varies from core to rim, decreasing from 11.2 to 2.1 mol% (see Table 2 in Medaris 1980).

Sample 2670 is jotunite granulite from Holsnøy, Norway, consisting of feldspar, garnet, clinopyroxene, orthopyroxene, and Fe-Ti oxides (see Table 2 [BA-48A] in Rockow et al. 1997). The sample is granoblastic with coarse grain sizes, 1–3 mm across. Pyroxene grains are well equilibrated with orthopyroxene [Mg/(Mg + Fe) = 0.59] occurring as lamellae in clinopyroxene [Mg/(Mg + Fe) = 0.66], which contains a significant proportion of non-quadrilateral components, mainly jadeite.

Sample 901 is a pyroxene andesite from the Rio Grande suite of calc-alkaline volcanics (see Table 1 and Figure 3 [Brushy Mt., BA1, RG-33] in Thompson et al. 1986). It contains euhedral phenocrysts of olivine, clinopyroxene, plagioclase, with smaller orthopyroxene phenocrysts set in a trachytic groundmass of plagioclase, clinopyroxene and Fe-Ti oxides. Clinopyroxene phenocrysts have compositions $En_{48-44}Fs_{16}Wo_{42-44}$. Bronzite xenocrysts have uniform compositions ($En_{80}Fs_{16}Wo_4$) and reaction rims of clinopyroxene and olivine (Thompson et al. 1986).

Sample M32 is a coarse-grained garnet-spinel lherzolite from Mingxi, China (Qi et al. 1995). Orthopyroxene and garnet are typically 2–4 mm in diameter with smaller clinopyroxene, olivine, and interstitial spinel. Orthopyroxene [Mg/(Mg + Fe) = 0.90–0.91] and clinopyroxene [Mg/(Mg + Fe) = 0.89–0.9] grains are equigranular and are not significantly zoned. (Hunter and Taylor 1982 in Qi et al. 1995).

Raman Experiments

Simplified polarization Raman measurements were done using a micro-Raman scanning spectrometer model U1000 (Jobin-Yvon/Instrument S. A.). The 514.5 nm line of an Ar^+ laser was used for excitation. The laser beam is linearly polarized at the sample. The spectral resolution varies from 3.6 to 3.1 cm^{-1} in the Raman shift range of 0–1250 cm^{-1}. Spectra were taken with the crystal initially oriented with its main axis (presumably its c axis) parallel to the polarization direction of the laser beam, and then again at 90° to the laser polarization. The relative intensities of each Raman peak in these spectra were then compared to determine the effect of crystal orientation. Strict and detailed polarization Raman measurements on quadrilateral pyroxenes are beyond the scope of this study.

Ordinary in-focus micro-Raman measurements were done by using a micro-Raman spectrometer model S3000 (Jobin-Yvon/Instrument S.A.) for relating peak position to chemical composition. The excitation source of this system is the 514.5 nm line of an Ar^+ laser for excitation and the laser beam is linearly polarized at the sample. The spectral resolution is ~7 cm^{-1} in the Raman shift range of 0–1250 cm^{-1}. The wavelength calibration of this Raman system was made by measuring the spectral lines of a standard Ne lamp and comparing them with published standard values. Accuracy is within ±1 cm^{-1} in the spectral range of interest. An 80× ultra-long working distance objective (0.85 N.A.) was used. This objective produces a condensed laser beam <1 μm in diameter. Actual

volumes analyzed in the samples are larger in diameter than the beam and vary from the spot to spot (Haskin et al. 1997). For lunar samples 15273,7039, 14161,7373, 14161,7080, QUE94281 and terrestrial sample Stillwater S2-123, spectra were taken on locations on thin or polished sections where electron microprobe analyses had been obtained. These spectra were taken with the excitation laser beam in focus at the surface of the sample. The wavelength reproducibility was checked using the Raman peak of a Si wafer every 2–3 hours interval in a working day. The drift was less than 0.5 cm^{-1} for the measurements of calibration set (15273,7039), and less than 1–2 cm^{-1} for other measurements.

Point-counting Raman measurements were done using a HoloLab-5000 Raman system (Kaiser Optical System Inc.) equipped with an automated scanning stage. The 632.8 nm line of a He-Ne laser and the 532 nm line of a frequency-doubled Nd:YAG laser were used for excitation. The laser beam is unpolarized at the sample. The spectrometer has a spectral resolution of ~4 cm^{-1}. A 20× long working distance objective (0.4 NA) was used for all measurements. It produces a condensed laser beam ~6 μm in diameter at the focal plane. The wavelength calibration of HoloLab-5000 system was established by a least-squares curve fitting of a set of measured Ne lines to standard values. The accuracy is better than 0.5 cm^{-1} in the spectral region of interest. The wavelength reproducibility was checked using the Raman peak of a Si wafer each working day, and was better than 0.3 cm^{-1} over several months. The purpose of these measurements was the simulation of automated point-counting traverses as anticipated for in situ Raman measurements on unprepared rock surfaces in the field, including on a planetary surface (Haskin et al. 1997). Automatic focusing is an unnecessary complication for a simple field Raman spectrometer, especially one that can be deployed by a robotic arm. In these experiments, the automatic scanning stage was used to reposition the sample laterally beneath the laser beam along a linear traverse, with spectra taken at selected intervals or on a rectangular grid. Thus, the laser was focused only once, at the first point of each linear traverse or grid. As no focusing adjustment was made before taking subsequent spectra, and because the sample surface was rough, the sample surface was usually a little above or a little below the laser focal plane at most points. At sampling points on which the beam is not focused on the sample, the analyzed volume of the sample is larger than at focus because of the divergence of the defocused laser beam. The signal to noise ratio of many spectra obtained in this way is lower than would have been the case for in-focus measurements. Also, because of the roughness of the rock surfaces, the sampling volumes in measurements on unprepared rock surfaces are expected to be somewhat larger than those on a polished section.